ERA report series

Paul Poli[1,2] and Pascal Brunel[3]

[1] ERA Project, ECMWF, Shinfield Park, Reading, UK

[2]. Now at Météo-France Centre de Météorologie Marine, Brest, France (email: paul.poli@shom.fr)

[3] Météo-France Centre de Météorologie Spatiale, Lannion, France

Series: ERA Report Series

A full list of ECMWF Publications can be found on our web site under:

http://www.ecmwf.int/en/research/publications

Abstract

This report presents an example of valorisation of two historical radiance datasets. In 1970 and 1971, the InfraRed Interferometer Spectrometer (IRIS) operated from the Nimbus-IV satellite. Even by today's standards, this Michelson interferometer was a hyperspectral sounder, with 862 channels. It covered wavenumbers between 400 and 1600 cm^{-1}(or 25.00–6.25 μm). Though without cross-scanning, this instrument predated by more than 30 years the current hyperspectral sounders such as AIRS on EOS-Aqua, IASI on Metop-A and -B, and CrIS on Suomi NPP.

The data collected by Nimbus-4 IRIS have so far not been used in global, multi-decadal, atmospheric re-analyses. Yet, these radiance data contain spectrally detailed information about our atmosphere's vertical structure and its constituents. Also, owing to the nature of the calibration problem acting on measurements of narrow spectral intervals, these radiance data have a great potential to serve as stable references in an assimilation scheme during the time period when they are available, or can be used to assess the quality of other atmospheric datasets, once the IRIS data quality has been understood and characterized.

The data from the Nimbus-4 IRIS experiment have recently been rescued from tapes by the NASA Goddard Earth Sciences Data and Information Services Center (GES DISC). With the aid of a state-of-the-art radiative transfer model, the EUMETSAT NWP-SAF RTTOV, we revisit this radiance dataset by comparing it with ECMWF reanalyses (ERA-40 and ERA-20C).

After cloud detection, we find in some spectral regions (e.g., 15 microns band) that the fit to the ERA-40 and ERA-20C reanalyses is below 1 K standard deviation in brightness temperatures. However, there are residual biases around 1 K in the window region which require further investigation.

The other dataset evaluated are radiances collected by Nimbus-VI HIRS, between August 1975 and March 1976. After applying simple quality controls, we find that the temperature sounding channels in the 15 microns band present no unexpected cross-scan field-of-view dependence. The data record is too short for assimilation and additional data from this experiment should be recovered.

Last, the report proposes that the series of infra-red sounders and imagers back to 1970 could help compare the first (IRIS) and current (IASI, CrIS) interferometers, with the help of the simultaneous nadir overpass technique. The magnitude of the discrepancy between forward- and backward-propagation of calibration corrections would then help refine the confidence placed in long-term trends derived from infra-red radiance data.

Contents

1   Introduction and motivations

The first pictures of our planet from space were taken on 24 October 1946 by a V2 rocket, launched from New Mexico, at an altitude of 105 km altitude (Reichhardt, 2006). On 1 April 1960, or about 14 years later, the TIROS-1 satellite captured what would go down in history as the first picture from satellite. TIROS-1 was placed into a 700 km altitude orbit by a rocket powered by an engine evolved by the Rocketdyne company from the German V2 engine technology. TIROS-1 sent images of the Earth with a regular schedule, and was dubbed "the first weather satellite". Today, or more than fifty years later, satellite observations have become a mainstay of our collective pool of environmental data. However, climate and weather scientists today are pressed to give responses to societal demands regarding the evolution of our climate. The natural approach

to answer a scientific question is to advocate for additional observational data, which justifies continuing and planning future missions for climate monitoring. There is another and complementary way, which consists in realizing returns on past investments. These old observational data can be exploited with the help of modern data analysis techniques. In atmospheric sciences, one such matching pair of opportunities is formed by, on the one hand, the 'historical' or 'heritage' satellite observations from the 1960s and 1970s, and, on the other hand, the modern tools that are Earth system reanalyses. In this paper we present a rationale for carrying out such work, and give an example with an ancestor of hyper-spectral sounding missions, the InfraRed Interferometer Sounder (IRIS) flown on the Nimbus-IV satellite (Hanel et al., 1970), and with the first instrument of the HIRS series, flown on Nimbus-VI.

The present paper is organized as follows. Section 2 proposes a rationale for bringing historical satellite data into the modern era of reanalyses. Section 3 gives an example of early satellite data work with the Nimbus-IV IRIS dataset. Section 4 shows comparison of this dataset with atmospheric reanalyses, projecting the latter into the IRIS observation space. Sections 5 and 6 present the Nimbus-VI HIRS dataset and results of comparison to reanalysis in observations space. Conclusions are in section 7.

We form the hope that the material presented here will stimulate the reader to embark on further studies in other areas of satellite data rescue.

2 Motivations for rescuing historical satellite data

In the following, most arguments refer to observations and reanalysis of the atmosphere, but similar arguments can be employed for the ocean, the land, and the biosphere. In an attempt to remain general, we employ "environment" to refer to either component interchangeably.

Reanalysis was advocated in the literature in the 1980s but for a variety of reasons. The First GARP Global Experiment (FGGE) undertaken between 1 December 1978 and 30 November 1979 was intended to support research on medium-range forecasting. It resulted in *de facto* reanalyses of that time period, aimed to be the best analyses possible for verification of forecasts. In 1983 Daley proposed reanalysis as a means of tracking progress in Numerical Weather Prediction. Bengtsson and Shukla (1988) proposed it as a method of constructing homogeneous, multivariate, internally consistent datasets of the atmosphere. Trenberth and Olson (1988) also saw reanalysis as a way of doing that but by exposing the effect of observation data changes on the climate record implied by the reanalysis dataset.

Reanalysis is essentially a two-step approach, although usually only the first of these two steps attracts visibility. First, observational data are confronted with a model of the environment of interest (for example, an atmospheric general circulation model), usually driven by initial, boundary, and forcing conditions. From the departures between the two, an analysis is drawn up, as corrections are made to the model state, within a process of data assimilation. The product is a gridded, time- and spatially complete, representation of the past environment. Because of changes in observation coverage and quality, the reanalysis datasets fall short of delivering the promise of Bengtsson and Shukla for all geophysical variables, and occasional discontinuities caused by data changes distract attention. However, under optimal conditions where sources of uncertainties are fairly represented, the analyzed products have lower uncertainties than any of the individual components, including observations, that enter the process, by the virtue of the filtering applied by data assimilation.

In a second step, the gridded representation thus produced, as well as the departures or (mis)fits between those products and the observations that went in it, can be analyzed by human expertise to pinpoint discrepancies (see for example, Simmons *et al.*, 2014). Such discrepancies can sometimes turn out to become points of contentions and feed scientific debate, but they point to much-needed improvements in either component of

the reanalysis system or its input. Such finding can be a missing source of variability in the underlying model. For example in ERA-Interim during large volcanic eruptions the assimilation of aerosol-contaminated satellite radiance observations caused the reanalysis to depart from radiosonde measurements of the atmosphere (Dee and Uppala, 2009). Another example is an inaccurate representation the central microwave frequency band, differing from that characterized with pre-launch measurements, for microwave channels (Lu and Bell, 2014).

Despite these many examples, these findings do not preclude the use of reanalysis data in several branches of science to better understand processes and variability. The reanalysis user and application survey, conducted early 2014 under auspices of an EU-funded project (Gregow *et al.*, 2015), attracted about 2600 respondents, among which about 1900 (1800, 1400) use temperatures and winds (respectively, pressure, precipitation) produced by reanalyses for their applications. The applications appear most varied, ranging from atmospheric and climate studies to energy-related studies and ship routing, but also include ecosystems modeling. One root cause for this global success is the fact that reanalyses use more observations of our environment than any other product alone. For example, between 1979 and 2012, ERA-Interim assimilated 40 billion observations, whereas any observational-only dataset, restricted by design to a single type or class of measurements, will only use a fraction of this number.

Since the advent of operational atmospheric sounding in 1979 with the TIROS-N satellite, satellite observations of our environment have been largely analyzed until the present times to monitor our current climate in the context of past measurements (e.g. Christy *et al.*, 2007). Figure 1shows the timeline of data records from polar-orbiting satellites assimilated in ERA-Interim until December 2009. The figure also shows entries for data records potentially available or known to have been collected at some point. There are quite a few missions before 1979 or TIROS-N, in particular those of the Nimbus satellite program (NASA, 2004). However, with a few notable exceptions, such satellite observations are now still largely under-exploited and remain as many untapped resources in global reanalysis. Notable exceptions are radiances from the Vertical Temperature Profile Radiometer on NOAA-2 to -5, used in ERA-40 (Uppala *et al.*, 2005) and JRA-55 (Kobayashi *et al.*, 2015), and ozone from the Nimbus-IV Backscatter Ultraviolet spectrometer (BUV), used in the NASA SBUV ozone version 8.6 product (McPeters *et al.*, 2013).

The reasons are quite obvious: none of these earlier missions came with the same level of consistency and quality offered by current operational-grade missions. They thus require more 'data work', for example to identify observations affected by gross errors. It is 'safer' for users to turn to qualified datasets such as generated by current or recent satellite missions, whose up-to-date data formats are also easier to use.

Yet, such ancient observations, even in relatively small numbers and although affected by larger instrumental errors than current higher-quality instruments, can still be used, provided their limitations are properly accounted for. This can be achieved at the observation time and location by the reanalysis framework described above, wherein the confidence given to observation information depends on the quality of such information. This does not preclude for the need to conduct advanced quality control to remove gross errors. The value of these observations is then to help extend the backwards reanalysis record, thereby enhancing the confidence that we can place in relating current environmental events into a longer timeframe. Another application, once the quality of these ancient data has been established, is to help assess quantitatively the uncertainties in climate datasets from climate model integrations or reanalyses.

MICROWAVE SOUNDERS AND IMAGERS (1972-)

+ MSU   TIROS-N   NOAA- 8   NOAA-10   NOAA-14
NOAA- 6   NOAA-11
NOAA- 7   NOAA-12
NOAA- 9

+ SSMT   DMSP F-7   DMSP F-8   DMSP F-14
DMSP F-9   DMSP F-12   DMSP F-15
DMSP F-10
DMSP F-11
DMSP F-13

* NEMS NIMBUS-5
* SCAMS NIMBUS-6   * AMSU-A   NOAA-15   NOAA-16   NOAA-17   NOAA-18   EOS-Aqua   METOP-A   NOAA-19

x SMMR   SEASAT NIMBUS-7   * AMSR ADEOS-2

x SSMI   DMSP F- 8   DMSP F-10   DMSP F-13   DMSP F-14   DMSP F-15
DMSP F-11

x TMI TRMM   x AMSRE EOS-Aqua

x MWS ERS-1   ERS-2   x MWR ENVISAT

x TMR TOPEX/POSEIDON   x JMR JASON-1   x AMR JASON-2

o SSMT2   DMSP F-11   DMSP F-12   DMSP F-14   DMSP F-15

o AMSU-B   NOAA-15   NOAA-16   NOAA-17

o MHS   NOAA-18   METOP-A   NOAA-19

Frequencies (application)
+ 60 GHz (Temperature sounding)
x 22 GHz (Integrated water vapor)
o 183 GHz (Water vapor sounding)
* 60 GHz and 22 GHz
⊛ 60 GHz, 22 GHz, 183 GHz

INFRARED IMAGERS (1964-)

HRIR   NIMBUS-1   NIMBUS-3
NIMBUS-2
MRIR NIMBUS-2 NIMBUS-3
THIR NIMBUS-4 NIMBUS-5   NIMBUS-7
NIMBUS-6

⊛ SSMIS   DMSP F-16   DMSP F-17   DMSP F-18
⊛ ATMS
⊛ MTVZA-GY

AVHRR   NOAA-7   NOAA-10   NOAA-14   NOAA-17   NOAA-18
NOAA-9   NOAA-12   NOAA-15   METOP-A
NOAA-11   NOAA-16

INFRARED LOW-RESOLUTION SOUNDERS (1969-)

SIRS   NIMBUS-3
NIMBUS-4
ITPR NIMBUS-5
VTPR NOAA- 2   NOAA- 5
NOAA- 3
NOAA- 4
SSH   DMSP F- 1   DMSP F- 4
DMSP F- 2
DMSP F- 3
HIRS NIMBUS-6
HIRS/2   TIROS-N   NOAA- 8   NOAA-10   NOAA-14
NOAA- 6   NOAA- 9   NOAA-12
NOAA- 7   NOAA-11

MODIS EOS-Terra
EOS-Aqua
VIIRS

INFRARED PRESSURE-MODULATED SOUNDERS (1970-2004)

SCR   NIMBUS-4
NIMBUS-5
PMR NIMBUS-6
SSU   TIROS-N   NOAA- 8   NOAA-11   NOAA-14
NOAA- 6
NOAA- 7
NOAA- 9

HIRS/3   NOAA-15   NOAA-17
NOAA-16
HIRS/4   NOAA-18   METOP-A   NOAA-19

INFRARED HYPERSPECTRAL SOUNDERS (1969-)

IRIS   NIMBUS-3
NIMBUS-4
SI-1 METEOR-27   IMG ADEOS-1   AIRS EOS-Aqua
METEOR-28   IASI METOP-A
CRIS

OZONE SENSORS (1970-)

BUV   NIMBUS-4
AE-E EXPLORER-55
TOMS   NIMBUS-7   METEOR-3   EARTHPROBE   ADEOS-1
SBUV NIMBUS-7
SBUV/2   NOAA- 9   NOAA-11   NOAA-14   NOAA-16   NOAA-18
NOAA-17   NOAA-19
EOS-Aura
MLS UARS
GOME ERS-2   MIPAS ENVISAT   GOME-2 METOP-A
SCIAMACHY ENVISAT   OMI EOS-Aura
OMPS

Legend

INSTRUMENT

SATELLITE

As assimilated in ERA-Interim

Known data record or mission

Data could not be located so far (lost forever?)

Instrument that continues the legacy for the coming years (launched after 2009, usually not used in ERA-Interim)

GPS RADIO OCCULTATION RECEIVERS (1995-)

BLACKJACK CHAMP   SAC-C
GRACE-A
TURBOROGUE GPS/MET   GRAS METOP-A
IGOR   COSMIC-1
COSMIC-2
COSMIC-3
COSMIC-4
COSMIC-5
COSMIC-6
TERRASAR-X

SCATTEROMETERS (1978-)

SASS SEASAT
AMI ERS-1
ERS-2
NSCAT ADEOS-1
SEAWINDS QUIKSCAT
ADEOS-2
ASCAT METOP-A

RADAR ALTIMETERS (1978-)

ALT SEASAT
RA ERS-1
ERS-2
RA-2 ENVISAT
NRA TOPEX/POSEIDON
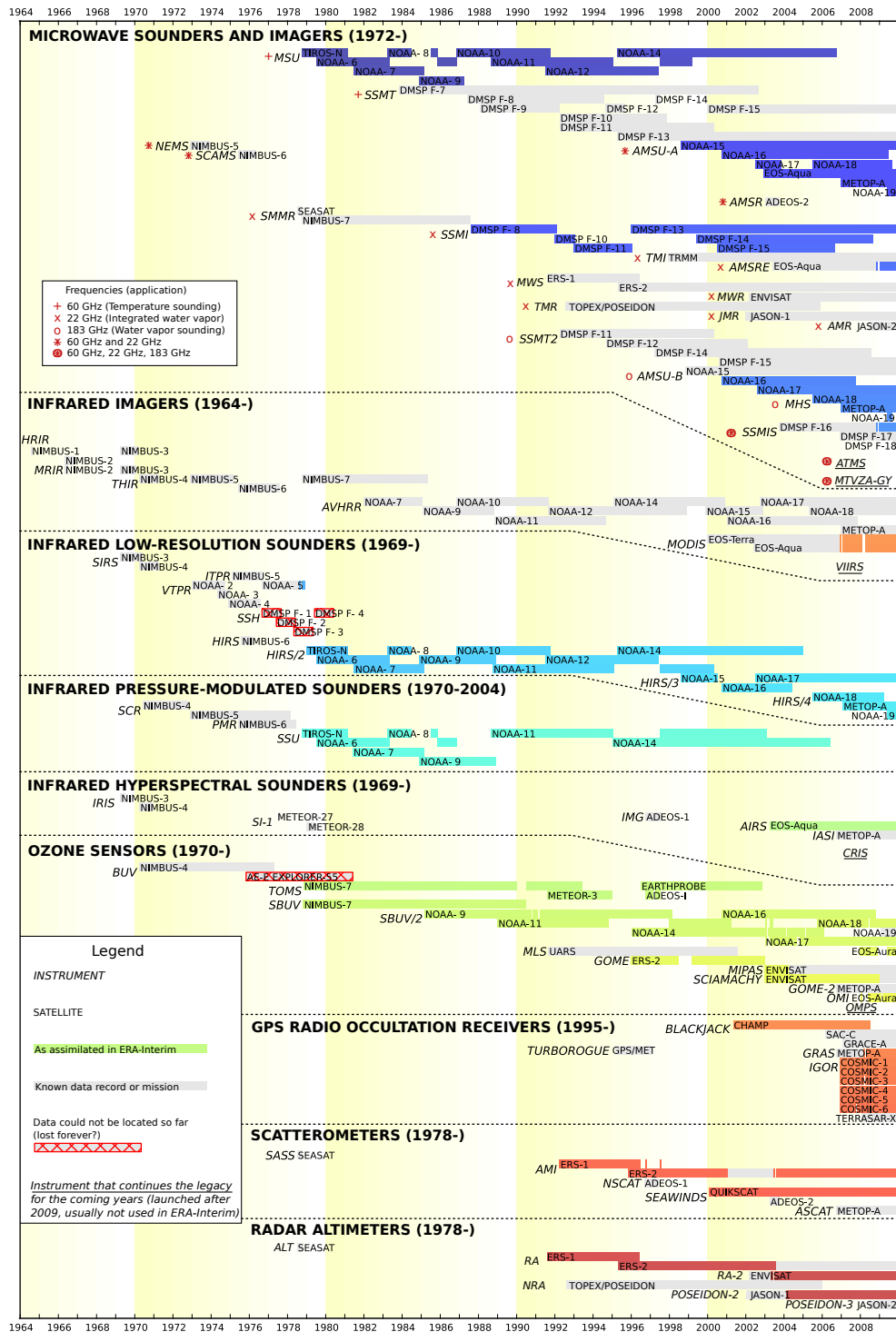POSEIDON-2 JASON-1
POSEIDON-3 JASON-2

Figure 1: Timeline of polar-orbiting satellite missions relevant for atmospheric reanalysis. Entries in colors show data assimilated in ERA-Interim until December 2009 while entries in grey indicate potential additional observation sources. See legend for additional details.
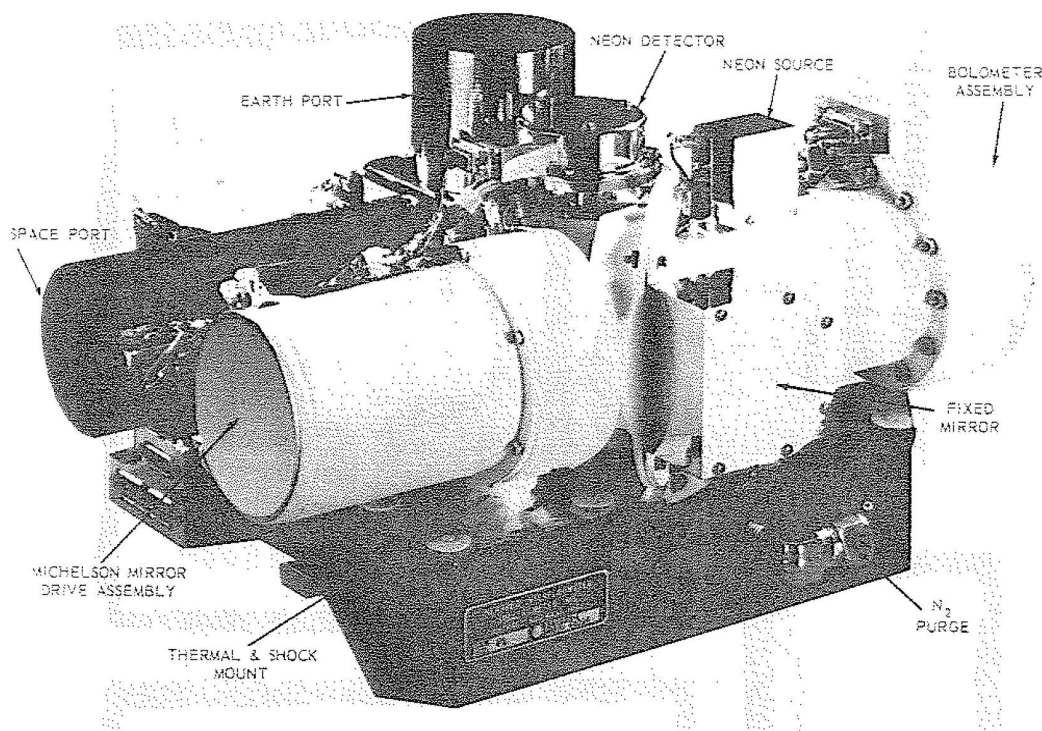
Figure 2: Schematic view of IRIS-D, from the Nimbus IV User's Guide (source: NASA)

3 A pioneering satellite instrument to observe the atmosphere: Nimbus-IV IRIS

In the 19th century when Michelson invented with Morley the optical instrument that would bear his name (Michelson and Morley, 1887), he probably did not foresee that this invention would be among the first man-made objects to leave the Solar system, onboard the Voyager-1 and Voyager-2 exploratory probes (launched in 1977 from Cape Canaveral). By the 1960s, the important concepts of Fourier transform spectroscopy had been well established, such as the relationship between mirror displacement and spectral resolution (e.g., Connes, 1958). Fourier transform spectrometers of the type of Michelson interferometers were flown onboard balloon-borne gondolas in the 1960s (e.g., Mucray et al., 1962). In 1966, a balloon carried a first version of the IRIS instrument (IRIS-A) which would later evolve and be taken to space. The IRIS-B flight model (flown on Nimbus-3), built by Texas Instruments (Dallas, Texas), was flown for testing on balloons and returned to NASA Goddard Space Flight Center in August 1968 (Bartman, 1968).

The IRIS-D model, shown in Figure 2, flew on the Nimbus-IV satellite (Figure 3). It covered the wavenumber range 400–1600 cm^{-1} (wavelengths 6.25–25 μm), with a nominal spectral resolution of 2.8 cm^{-1} apodized (1.4 cm^{-1} unapodized). It featured no cross-scanning, and the footprint was about 94 km (Hanel et al., 1970).

The data from the Nimbus-IV satellite have survived the perils of time thanks to the vision of NASA to preserve its data holdings. After preservation by the NASA Space Science Data Center (NSSDC) for decades, these data were rescued from ageing tapes by the NASA Goddard Earth Sciences Data and Information Services Center (NASA GES DISC). The raw data format is described by the Nimbus-IV user's guide (Nimbus project, 1970). The dataset includes calibrated spectra, but also instrument health status metadata.
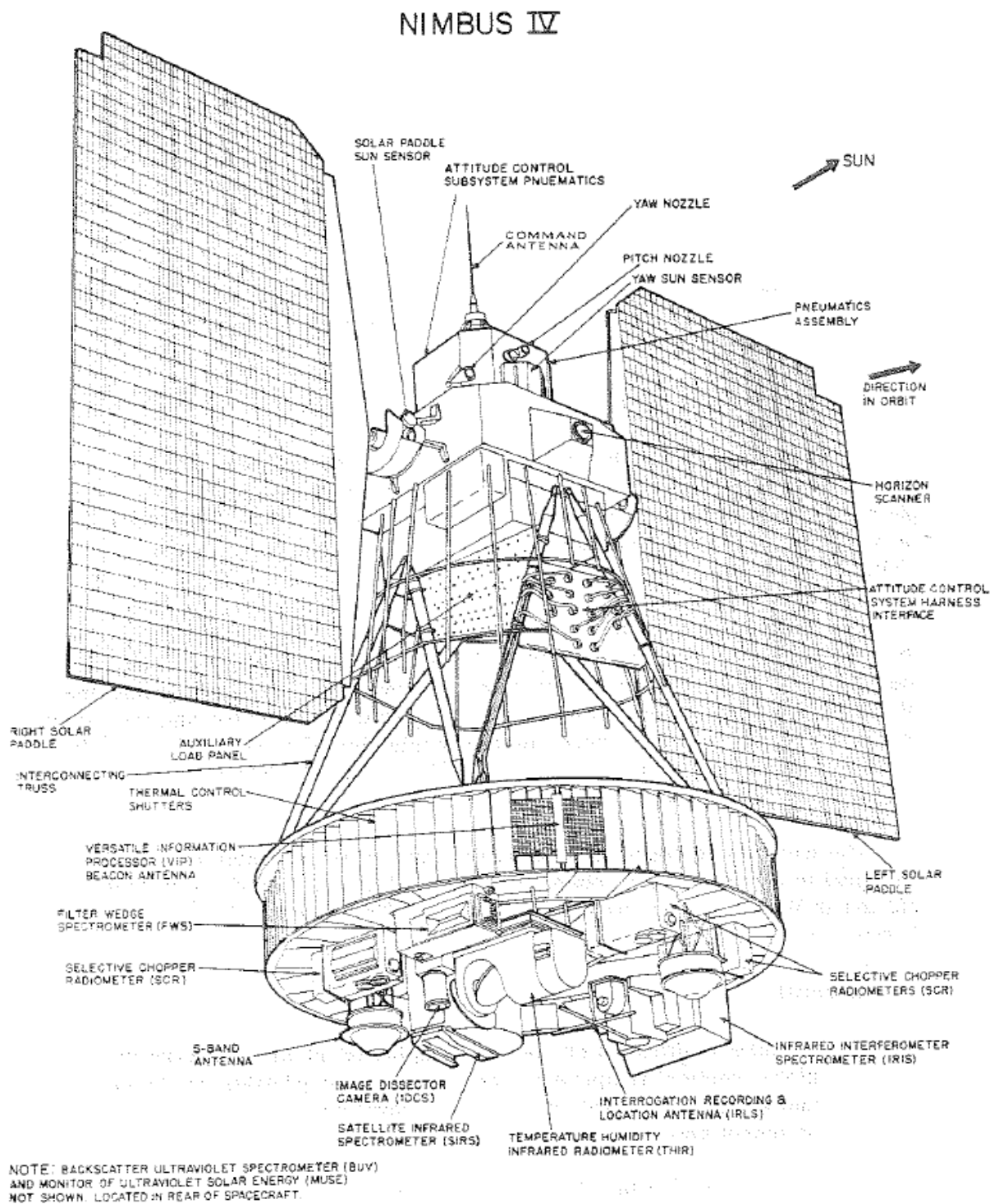
Figure 3: Schematic view of Nimbus-IV, from the Nimbus IV User's Guide (source: NASA)

Attribute	Unit or format	Range of values found in the data
Latitude	degrees North	-80.17 to 80.17
Longitude	degrees East	-180.0 to 179.99
Date	YearMonthDay	19700409 to 19710130
Time	HourMinuteSecond	7 to 235955
Channel number	none	1 to 862
Wavenumber	cm^{-1}	400.5 to 1600.7
Radiance	$W/m^2/ster/\ cm^{-1}$	-79.36 to 423,178.62
Brightness temperature	K	54.17 to 21,222.54

Table 1: List of attributes retrieved from the native Nimbus-IV IRIS data files and transferred into ODB, along with a summary of the data found. Note: the range of brightness temperatures is only for positive radiances

3.1   Raw dataset

Data pre-processing for this study is as follows. First, the data are read from their native format by a program provided by James E. Johnson (NASA GES DISC) running on IDL (a software produced by the Exelis Visual Information Solutions company). This step is crucial (without it, one cannot easily read the data). It must be noted that the author of the reading program identified few, but nonetheless unexplained differences between the actual data and the format described in section 4 of the Nimbus IV User's Guide (Nimbus project, 1970).

In a second step, the resulting data are written into a compressed numerical format supported by the Observation DataBase Application Programming Interface (ODB API). This numerical format allows archiving on the ECMWF Observation Feedback Archive (OFA) facility (Kuchta, 2009) and launching Structured Query Language (SQL) computations and searches. The efficiency of the ODB API compression allows to stream large amounts of observations.

At this point, only the information listed in Table 1 is preserved into ODB data files. Note, the longitudes are originally found with a convention opposite to current practice, so the sign is thus reversed (to adopt the more common convention of longitudes East positive). The convention of longitudes West positive is somehow still the default in other softwares (e.g., McIDAS: http://www.ssec.wisc.edu/mcidas/doc/users_guide/cur Brightness temperatures are calculated from the radiances in the process, assuming that each channel collects monochromatic radiation at the following wavenumbers:

$$\tilde{v}_i = \tilde{v}_0 + (i-1)\Delta\tilde{v} \tag{1}$$

where $\tilde{v}_i$ is the wavenumber for channel number i (from 1 to 862), and $\tilde{v}_0$ and $\Delta\tilde{v}$ are read from the data. Both are found to be invariant throughout the dataset: $\tilde{v}_0$=400.470459 cm^{-1} and $\Delta\tilde{v}$=1.390523 cm^{-1}. The total size of the ODB files created at this point is about 7 Gb, containing 663,137 spectra.

Using the ODB SQL capabilities enables to find out quickly basic properties, such as data range (minimum and maximum), without any need for complicated software (see Table 1). Applying also simple queries to bin the information by month, Figure 4 shows the monthly data count of spectra, around 55,000 per month between April and December 1970. Binning the data by location, Figure 5 shows the complete coverage achieved by the Nimbus-IV IRIS experiment. Note the relative paucity of data at the location of the South Atlantic Anomaly (over Brazil), prone to electromagnetic radiation perturbation, as it was coming to be understood at the time. This anomaly had been discovered with the Van Allen radiation belts in 1958 (Van Allen, 1958) by the first US satellite in space, Explorer 1, officially called 'Satellite 1958 Alpha' at the time. Satellites today carry radiation shielding to protect their electromagnetic equipments, however there are still occasional reports, though rare

Figure 4: Monthly count of 862-channel spectra

now, of failures on spacecrafts when crossing over this anomaly.

3.2   Simple quality controls

Figure 6 shows the complete set of calibrated radiances found in the dataset. At low wavenumbers, one recognizes the P and R sides of the 15 μm carbon dioxyde (nu2 vibrational mode at 667 cm^{-1}). Other salient features of the atmospheric spectrum are also visible, such as the 9.6 μm ozone band (constituted by the nu1 and nu3 vibrational modes at 1110 and 1043 cm^{-1}) and the 7.6 μm methane band (nu4 vibrational mode at 1306 cm^{-1}). As indicated in Table 1, the dataset contains a number of negative radiances. These are obviously unphysical, but not unexpected given instrument noise. Of concern however are a series of spectra which resemble perfect blackbody spectra, probably mistakenly encoded as atmospheric measurements.

To validate this hypothesis, Figure 7 shows the complete set of brightness temperatures, computed only for positive radiances. Horizontal streaks cluttered around 2 sets of temperatures appear. The first set of 'flat' spectra is tightly concentrated near 285 K (within 1K), which is in fact the temperature of the (warm) blackbody inside the instrument. The second set of suspicious spectra lie in the range 218–251 K, but are all nearly 'flat'. This allows to derive a first series of quality controls, collectively referred as QC1 hereafter: radiances must be positive and below 220 W/cm**2/ster.cm, the spectrum of brightness temperatures must present a minimum variability (maximum minus minimum greater than 19 K; this value is chosen after inspecting the spectra with suspiciously low variability), and the 677 cm^{-1} brightness temperature must remain in the range 150–250 K. The data passing QC1 are shown in Figure 8. As expected, the problems identified earlier have been removed.

Number of Nimbus-4 IRIS profiles per 1 degree x 1 degree
1 2 3 4 8 16 20 24 28 32 36 40 44 48 52
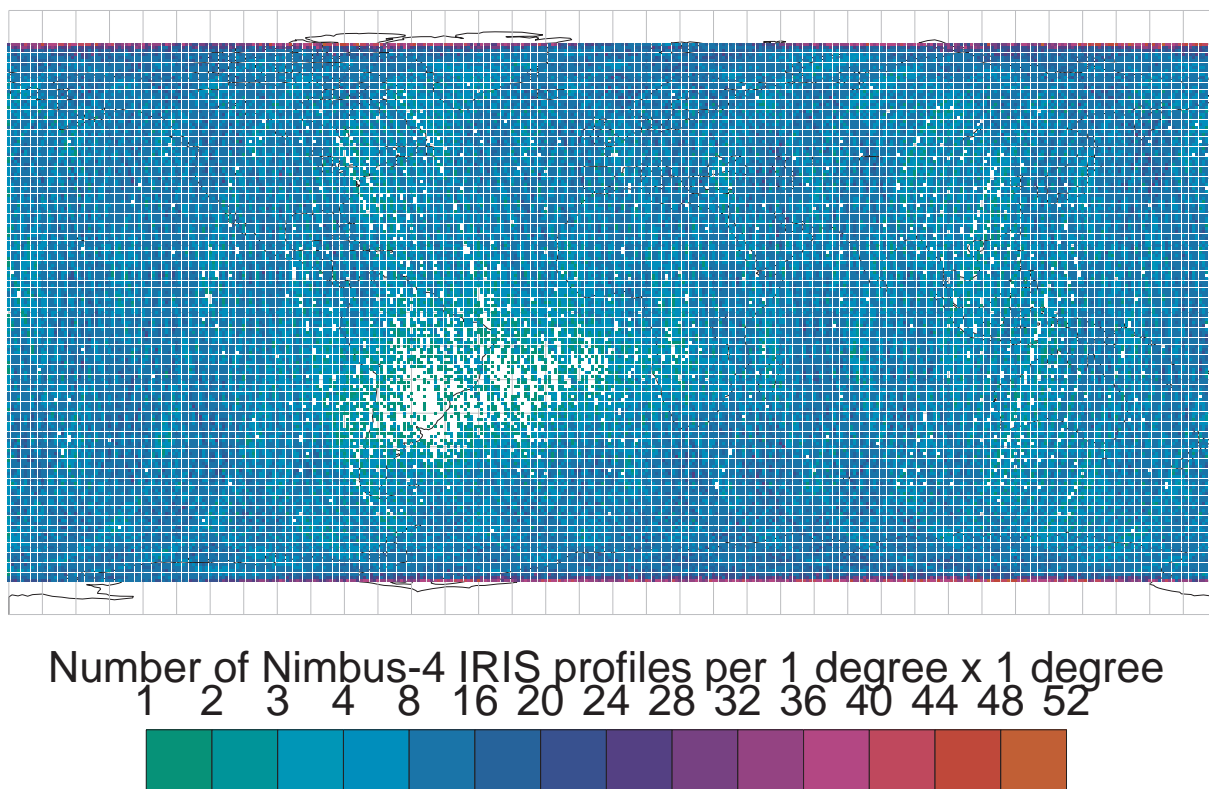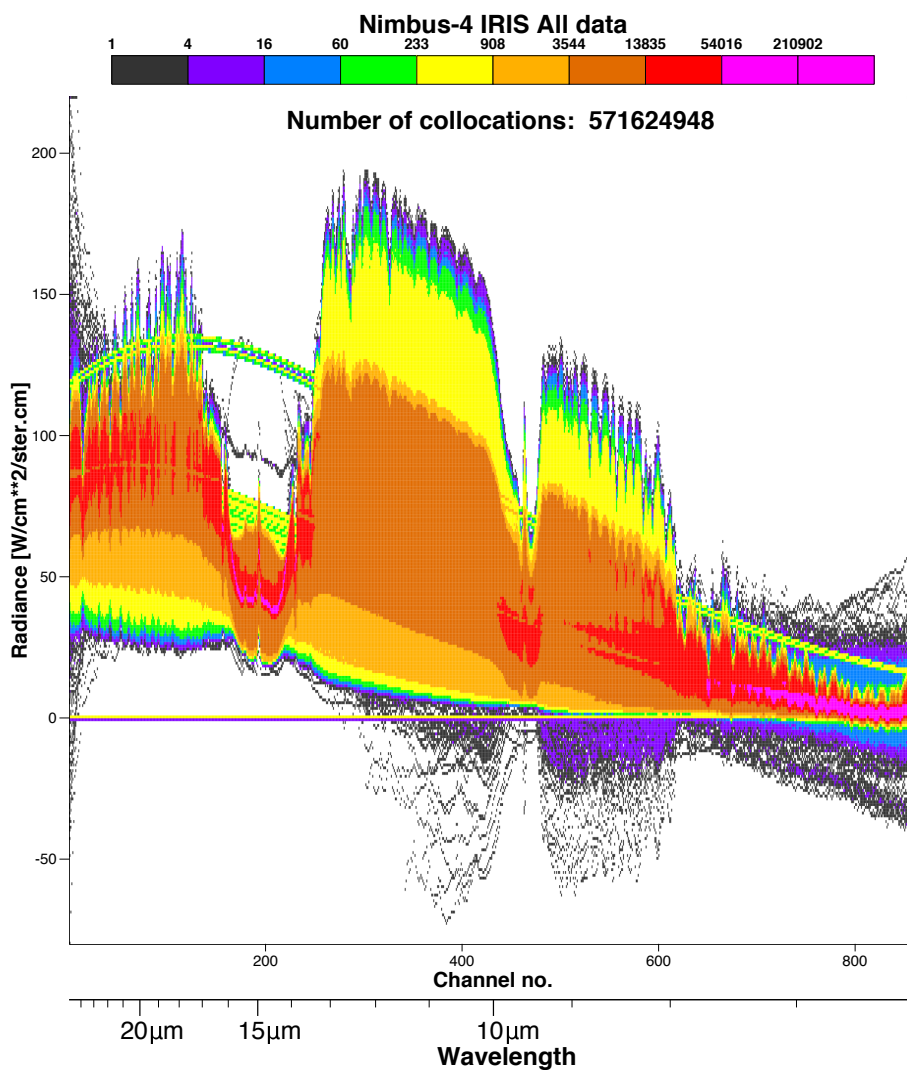
Figure 5: Map of count of Nimbus-IV IRIS soundings

Figure 6: Density plot of all calibrated radiance observations found in the Nimbus-IV IRIS dataset. Total number of spectra is 663,138.
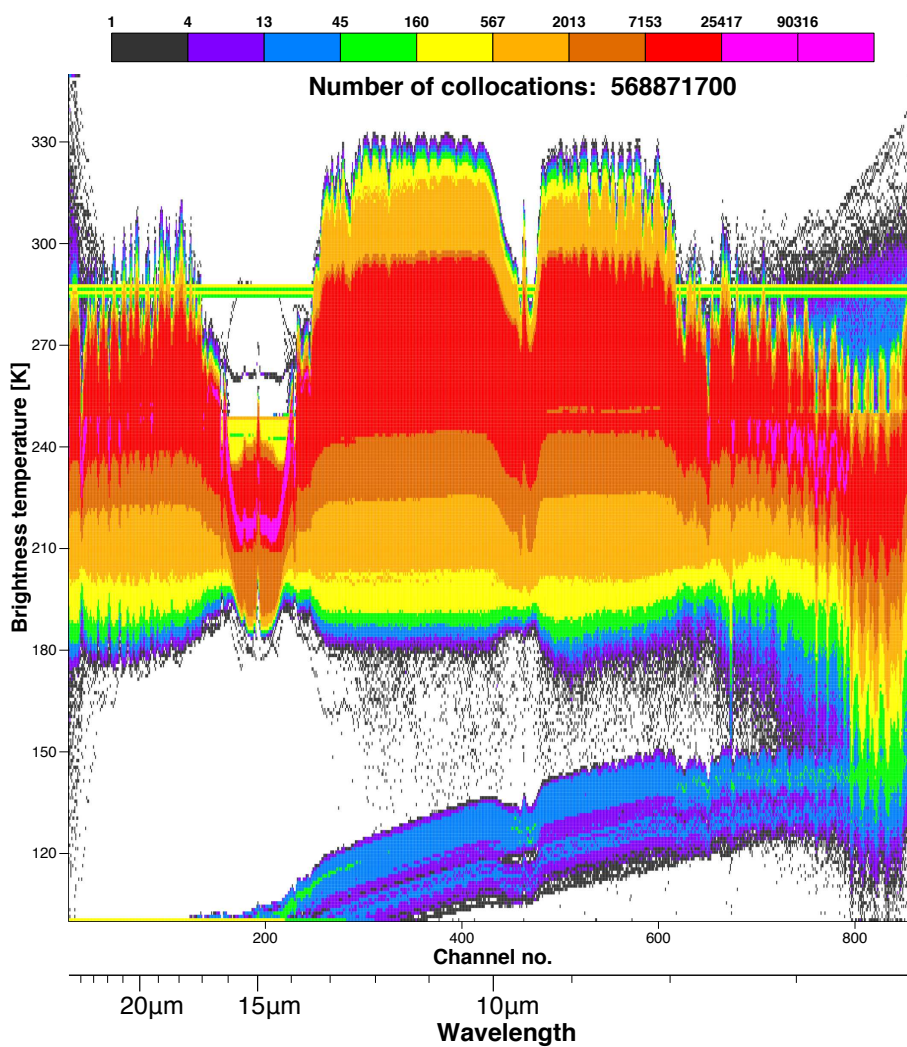
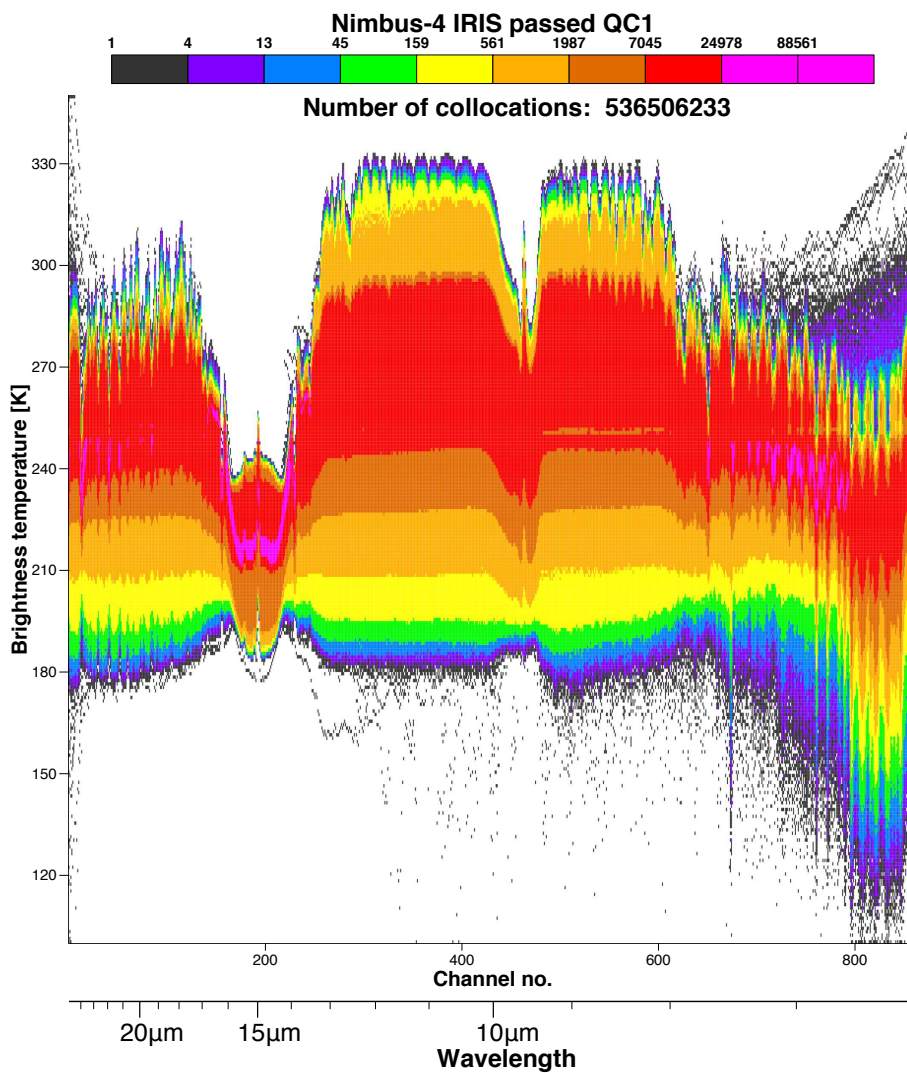*Figure 7: Density plot of all brightness temperatures (only computed for positive radiances).*

Figure 8: Density plot of all brightness temperatures for the data passing QC1.

3.3   Geolocation

Figure 9 shows monthly maps of the 623,619 spectra that pass QC1. The channel shown is chosen in the window region, and the map shows the maximum brightness temperature in each 1 degree x 1 degree bin. In spite of the possible presence of clouds throughout the record at some locations, ice regions are clearly visible, and so are transitions between land and sea. Without cloud clearing, it is not possible at this point to assess the geolocation accuracy, but generally the latitude and longitude specifications appear correct.

However, a careful inspection of the maps shows that January 1971 contains anomalous orbit tracks. This is better seen in Figure 10, coloring the orbit tracks by the day of the month. The incorrect geolocation only affects the first 8 eight days of January 1971. It seems unrealistic that Nimbus-IV would have changed orbits for a couple of days during its mission.

3.4   Instrument health status metadata

The dataset available from NASA GES DISC features, as documented in the Nimbus IV user's guide, 9 types of records. The 1st and 9th types contain summary information. The 8th type of records contains calibrated spectra but also, for each spectrum, temperatures of: the bolometer (two values, one being from the redundant sensor – we find that the first of the two bolometer temperatures seems to be encoded in degrees Celsius, whereas all other temperatures are in Kelvin), the blackbody (plus a redundancy), the beamsplitter, the mirror drive motor, the Image Motion Compensation and Calibration (IMCC) subassembly, and the cooling surface. It also contains IMCC position (usually 0), calibration transducer, and voltage calibrations for +0.6V, 0.0V, and -0.6V, all found very stable, close to these nominal values. All these metadata are shown in Figure 11. To understand the relevance of all these measurements, it helps to consider the diagram shown in Figure 12. It seems that the temperature raised for the whole instrument towards the end of the mission, starting October 1970. Understanding this gradual increase in temperature is probably within reach of current modelling capabilities: for example, using a model of the spacecraft carrying the instrument, Kunkee et al. (2008) conducted ray-tracing simulations to assess accurately the sensor exposure for a microwave imager. Around the same time of these temperature changes, we also notice that the -0.6V calibration degrades slightly.

The record types 2 to 7 contain spectra of cold calibration count, warm calibration count, average responsivity, Noise Equivalent Radiance (NER), average instrument temperature, and standard deviation of instrument temperature. All the values found in the dataset for these respective quantities are shown in Appendix B. We find in particular that the noise equivalent radiance features sometimes very large values and this may be used to screen out poor quality data.

All this information is useful to isolate events when the instrument appeared to function outside of normal range. The following quality controls are added: data are removed if the cooling surface temperature, the IMCC subassembly temperature, or the mirror temperature is below 240 K, or if the IMCC position is greater than 3, or if the +0.6V (0.0V, -0.6V) calibration is outside the range 0.59–0.65 (respectively: -0.01 to 0.05, -0.61 to -0.55), or if the transducer calibration is outside the range 0.034–0.040. This set of criteria, along with the rejection of days 1 to 8 January 1971, forms the second series of quality controls, collectively referred as QC2 hereafter.

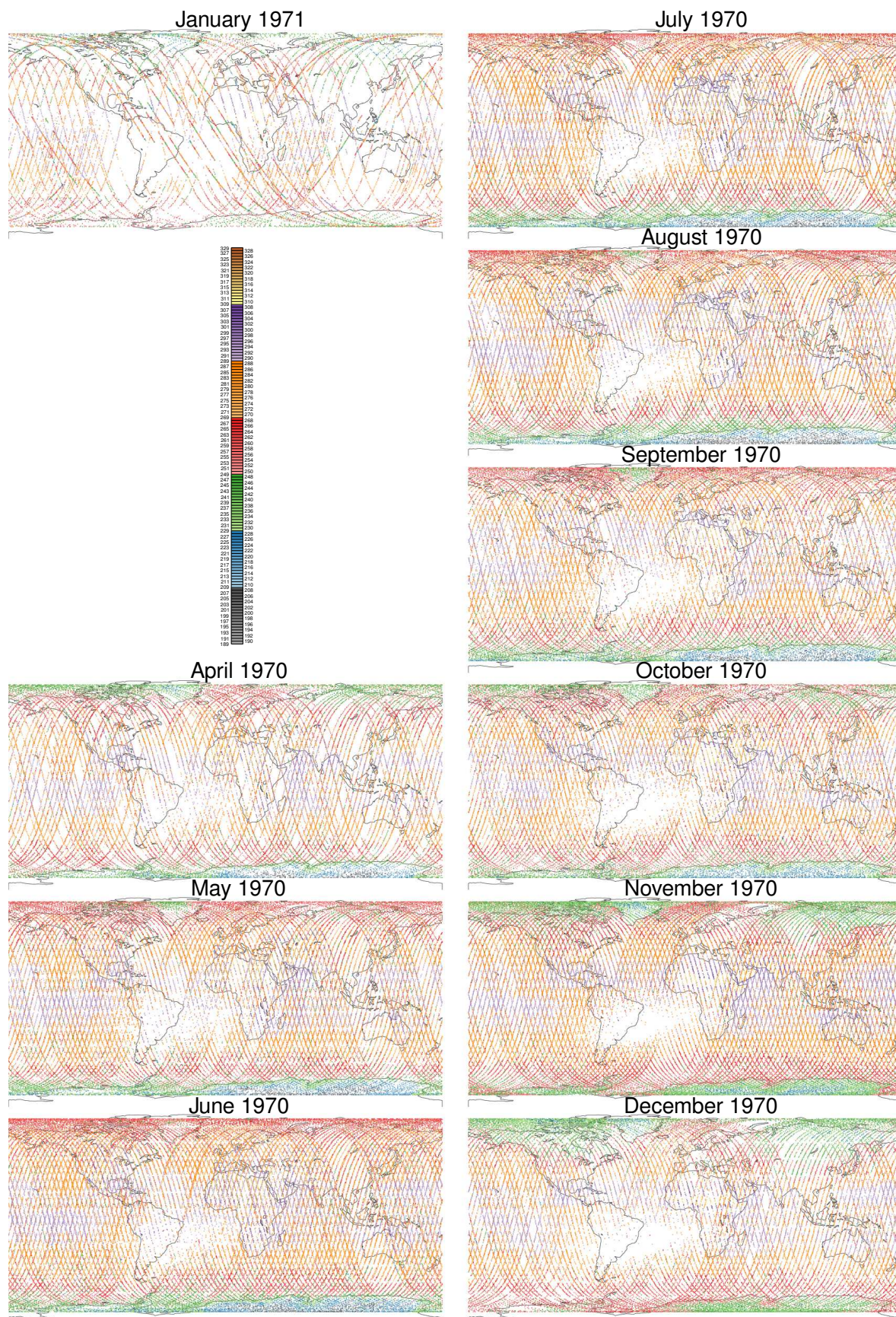The data passing QC1 and QC2 are shown in Figure 13.

Figure 9: Maps of maximum brightness temperature observations passing QC1 for channel number 360 (899.67 cm^{-1}, similar to HIRS window channel 8).
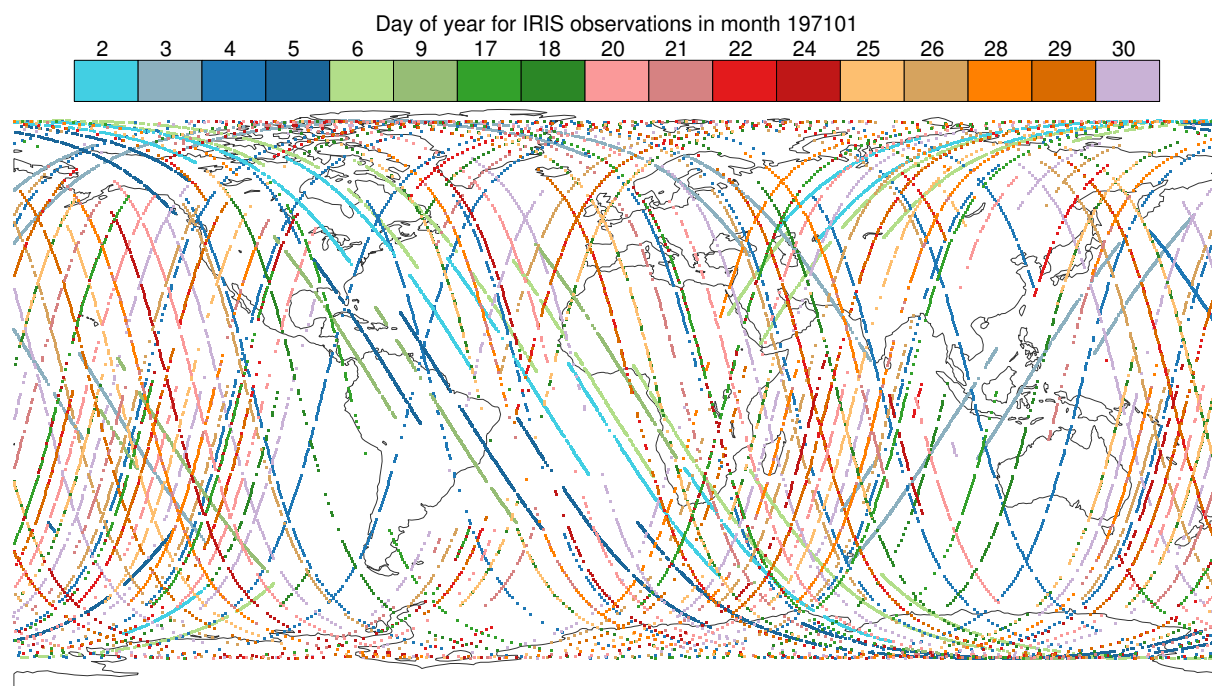
Figure 10: Maps of observations collected by IRIS during the month of January 1971 (the instrument did not work on all days). Orbit tracks for days 2 to 9 appear to be incorrect.

4 Comparison of Nimbus-IV IRIS with atmospheric reanalyses

Evaluating a dataset is greatly helped by a comparison with other datasets. To this end we use atmospheric reanalyses as input to a radiative transfer model, such as RTTOV (Saunders et al., 2013), and compare the computations of simulated Nimbus-IV IRIS spectra with actual observations. We consider here two reanalyses, ERA-40 (Uppala *et al.*, 2005) and ERA-20C (Poli *et al.*, 2015). The comparison procedure works as follows, for a given set of Nimbus-IV IRIS observations. First, we retrieve from the ECMWF archive two-dimensional fields of temperature, specific humidity, and ozone at all the vertical levels produced by the reanalysis (60 levels for ERA-40, 91 levels for ERA-20C), at the native reanalysis horizontal resolution (for both reanalyses: reduced Gaussian grid of truncation T159, or approximately 125 km), and at the time resolution of the reanalysis product (6-hourly for ERA-40, 3-hourly for ERA-20C). Second, we interpolate bi-linearly in space to each Nimbus-IV IRIS observation location the meteorological reanalysis fields closest in time so as to obtain a multivariate profile of temperature, specific humidity, and ozone at sub satellite point. Third, we pass these profiles to RTTOV which then calculates simulated Nimbus-IV IRIS radiances.

4.1 Prior RTTOV preparations

The version of RTTOV used here is RTTOV v11.2. The Nimbus-IV IRIS Instrument Spectral Response Function is calculated in wavenumber space (ISRF-1C) by taking the Fourier transform of the apodization function specified in the Nimbus-IV User's Guide (page 79, shown in Figure 14). The apodization function is calculated for 51200 samples, with a resolution of 0.195 μm in order to get a final spectral resolution of 0.010 cm^{-1}. The ISRF-1C, shown in Figure 15, is defined over the range [-16, 16] cm^{-1}, with a full width at half maximum of 2.50 cm^{-1}. The same ISRF-1C is used for all channels. There are 862 channels from 400.470459 to 1597.710693 cm^{-1} in the calibrated dataset. The spectral sampling is 1.390523 cm^{-1}. Figure 15 includes a

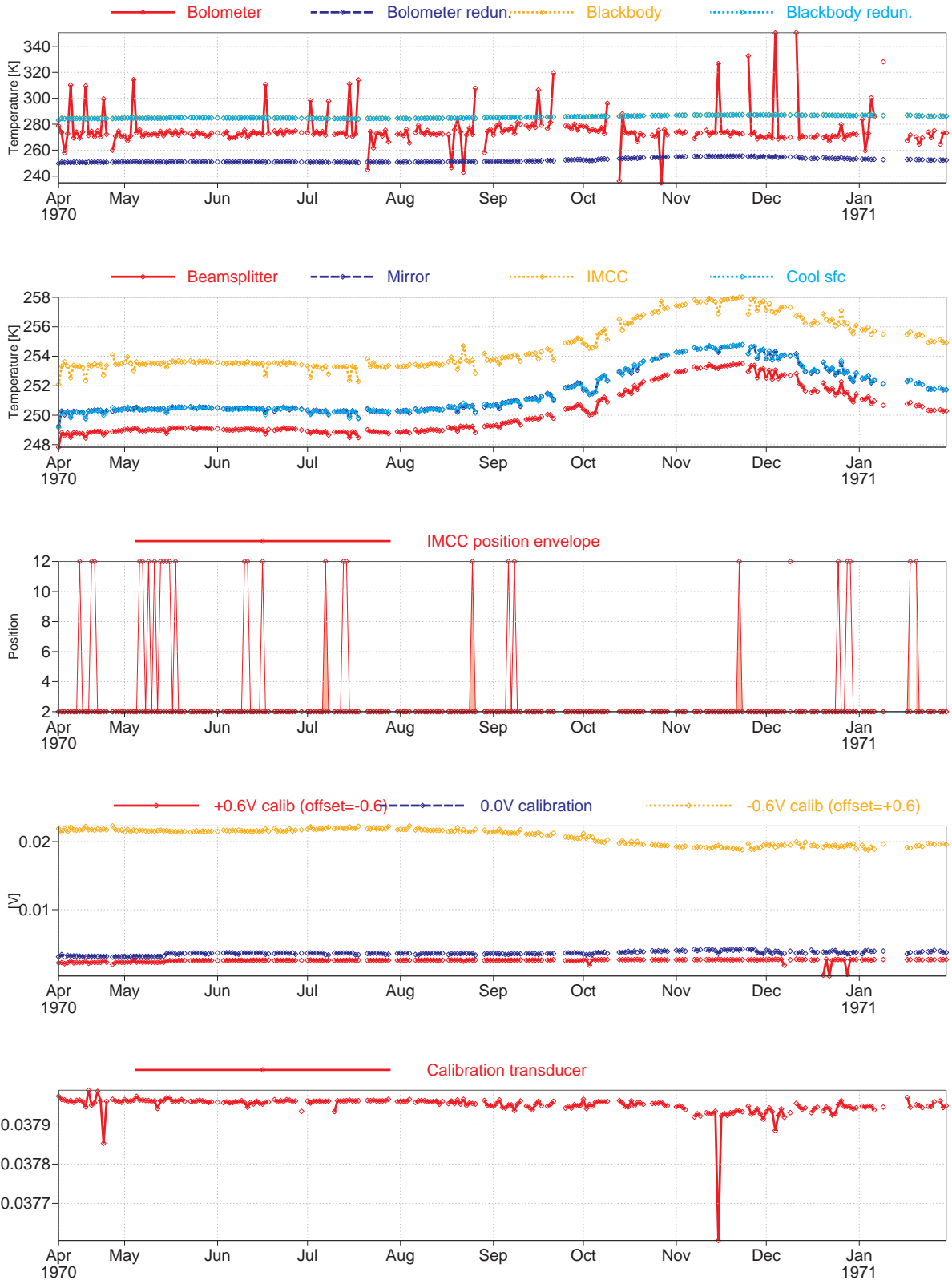**IRIS instrument status monitoring**

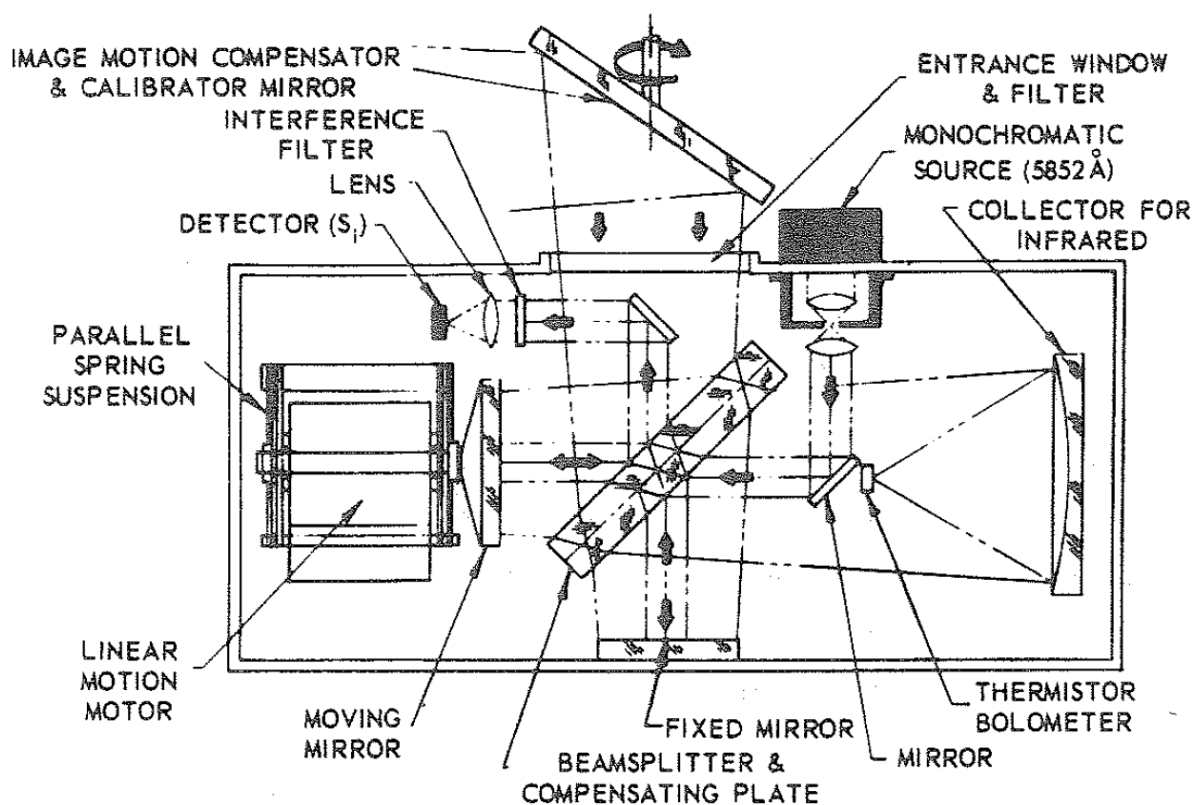*Figure 11: Instrument health status metadata found in the IRIS dataset record type 8.*

Figure 4-3. Schematic Diagram of Michelson Interferometer. The Monochromatic Source is a Neon Discharge Tube

Figure 12: Schematic view of the Michelson inteferometer, from the Nimbus IV User's Guide (source: NASA)
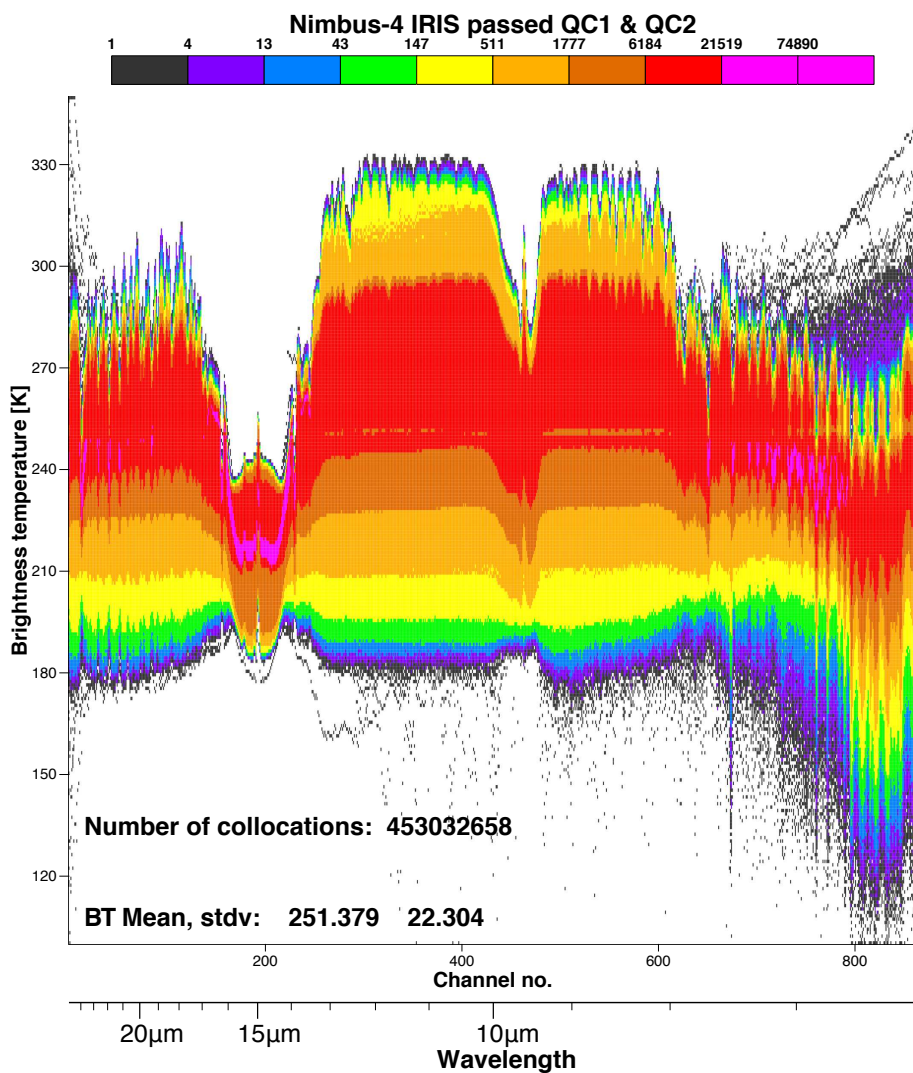
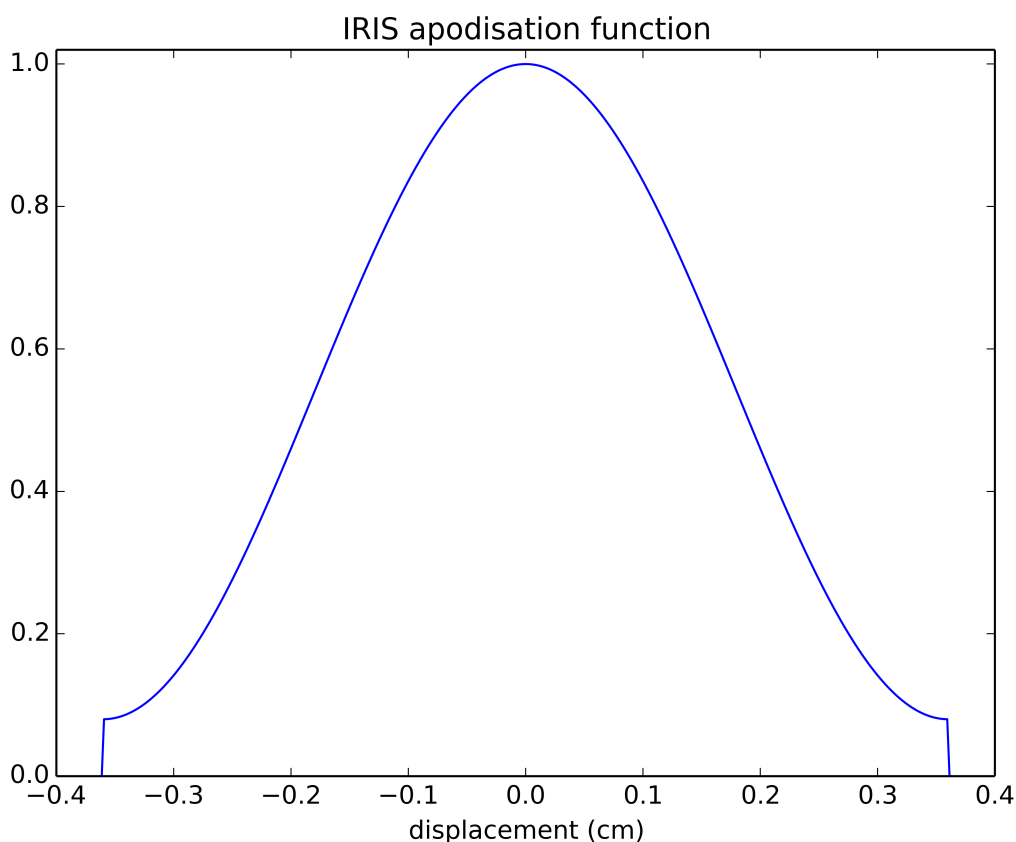*Figure 13: Density plot of all brightness temperatures for the data passing QC1 and QC2.*

Figure 14: Apodization function used for Nimbus-IV IRIS

comparison of Nimbus-IV IRIS ISRF-1C with that of current infrared interferometers such as IASI and CrIS.

The ISRF-1C is applied to the line-by-line transmittances of the RTTOV training set with variable carbon dioxyde. The Line-By-Line Radiatve Transfer Model (LBLRTM, Clough et al., 2005) v12.2 with Atmospheric and Environmental Research (AER) v3.2 spectroscopic database are used to build the line-by-line transmittance database. The training set is designed for the thermal infra-red in the range 3–50 μm, with some margins in the line-by-line calculations (wavenumber range 150–3350 cm^{-1}).

As the atmospheric concentration in carbon dioxide has changed substantially since the 1970s, the RTTOV coefficients need to be based on concentrations realistic at that time. This is almost achieved by using the capability of RTTOV to use as input predictor a profile of carbon dioxide. However, the current minimum carbon dioxide concentration acceptable by RTTOV at the surface is 372 ppmv, which is larger than the concentration in 1970, at about 325 ppmv. Note, RTTOV is able to manage user input profiles with concentrations lower than the training dataset, but this option should be handled with care. Future RTTOV training runs should address this issue raised by historical instruments by widening the range of acceptable carbon dioxyde input concentrations.
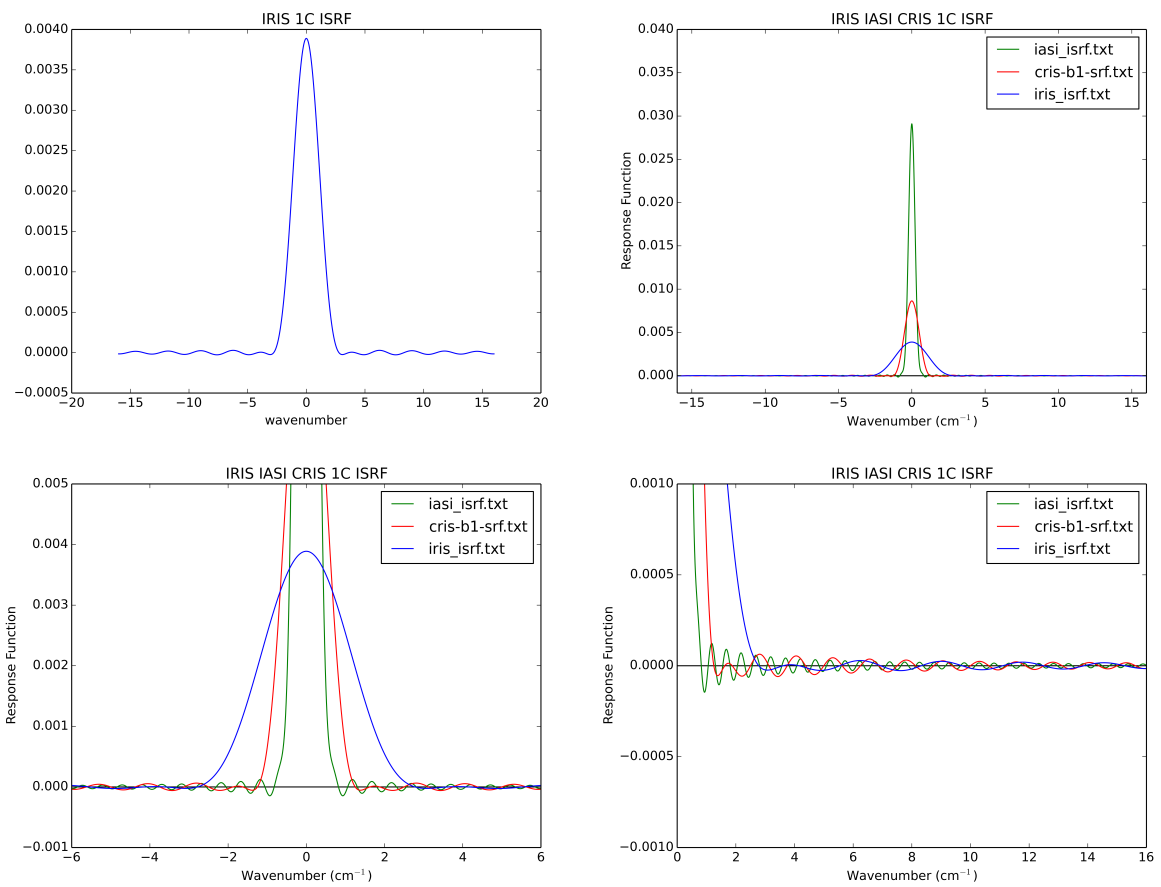
Figure 15: Instrument Spectral Response Functions for Nimbus-IV IRIS (1970) and selected current hyper-spectral infrared interferometers (2006 onwards)

4.2 RTTOV application

A first application of RTTOV is shown in Figure 16, to estimate the typical simulated brightness temperatures for a mid-latitude atmosphere. Unfortunately at the time of application the IRIS radiative transfer coefficients were not reliable below 511 cm^{-1} (the remainder of the report uses however coefficients that extend to 400 cm^{-1}), so the horizontal axis in Figure 16 only covers channels 81–862. Reading from the right vertical axis, the main spectral features found in the observations are represented. Another application is to estimate for each channel the weighting function (as the derivative of the transmittance with respect to the logarithm of pressure), and then summarize this information by extracting from the weighting function profile the pressure range where the weighting function reaches maximum values. Figure 16, left vertical axis, shows, as expected, that channels at the center of the absorption lines sense regions located higher in the atmosphere, with a gradient on both sides of the 15 μm band, which can hence serve for atmospheric sounding. The window region 800–1000 cm^{-1} is clearly visible. For future reference the figure also features at the top another horizontal axis showing the Nimbus-IV IRIS channel number.

4.3 Result of comparisons with reanalyses

Figure 17 shows density plots of differences between Nimbus-IV IRIS brightness temperatures and simulations carried out from ERA-40 atmospheric profiles at the location and near the time of the observations. Only the spectra that passed QC1 are considered in the top panel. The effect of QC2 is visible in the bottom panel, removing spectra that present departures upwards of 60 K in the window region. The spread of the differences is more narrow near the center of the 667 cm^{-1} band, but otherwise for most channels we observe the cold effect of clouds, with departures down to -90 K or below.

A visual inspection suggests that some spectra probably failed calibration. To remove them, we compute the linear correlation (r), for each spectrum, between the simulated values and the observed ones. This correlation is computed considering the channels 81–500 where the instrument noise is not too large. This channel range is based on the noise equivalent spectra for the entire mission, shown earlier in Figure 38. Figure 18 shows the density plot of correlations using ERA-20C simulations or ERA-40 simulations, considering all spectra that passed QC1. There is generally good agreement between the two until correlations of about 0.8, at which point the two can indicate different correlations. We hence define as QC3 the removal of spectra where correlations with ERA-40 and ERA-20C are both below 0.8 (as long as the observed spectrum features a correlation with ERA-40 or ERA-20C that exceeds 0.8, it passes QC3).

The resulting set of observations is shown in Figure 19. The top panel indicates that the effect of QC3 is to remove outlier spectra that were visible earlier in Figure 18 at channels 600 and above. Comparing also with Figure 18, the bottom panel of Figure 19 shows that many cold departures have been removed, possibly because cloud-affected spectra feature lower correlations with clear-sky radiative calculations. This may then indicate that the correlation test has removed some possibly 'good' but cloudy scenes; for the highest-peaking channels in the 15 μm band, such rejected data may otherwise be used for stratospheric and mesospheric studies. However, this test is possibly still useful to remove cloud-contaminated data. The next step is to conduct a cloud detection.

4.4 Cloud detection

One aspect requiring attention before further use of infra-red observations is cloud contamination. To this end, we apply the ECMWF Aerosol and Cloud Detection Software (Eresmaa, 2015), which relies on the
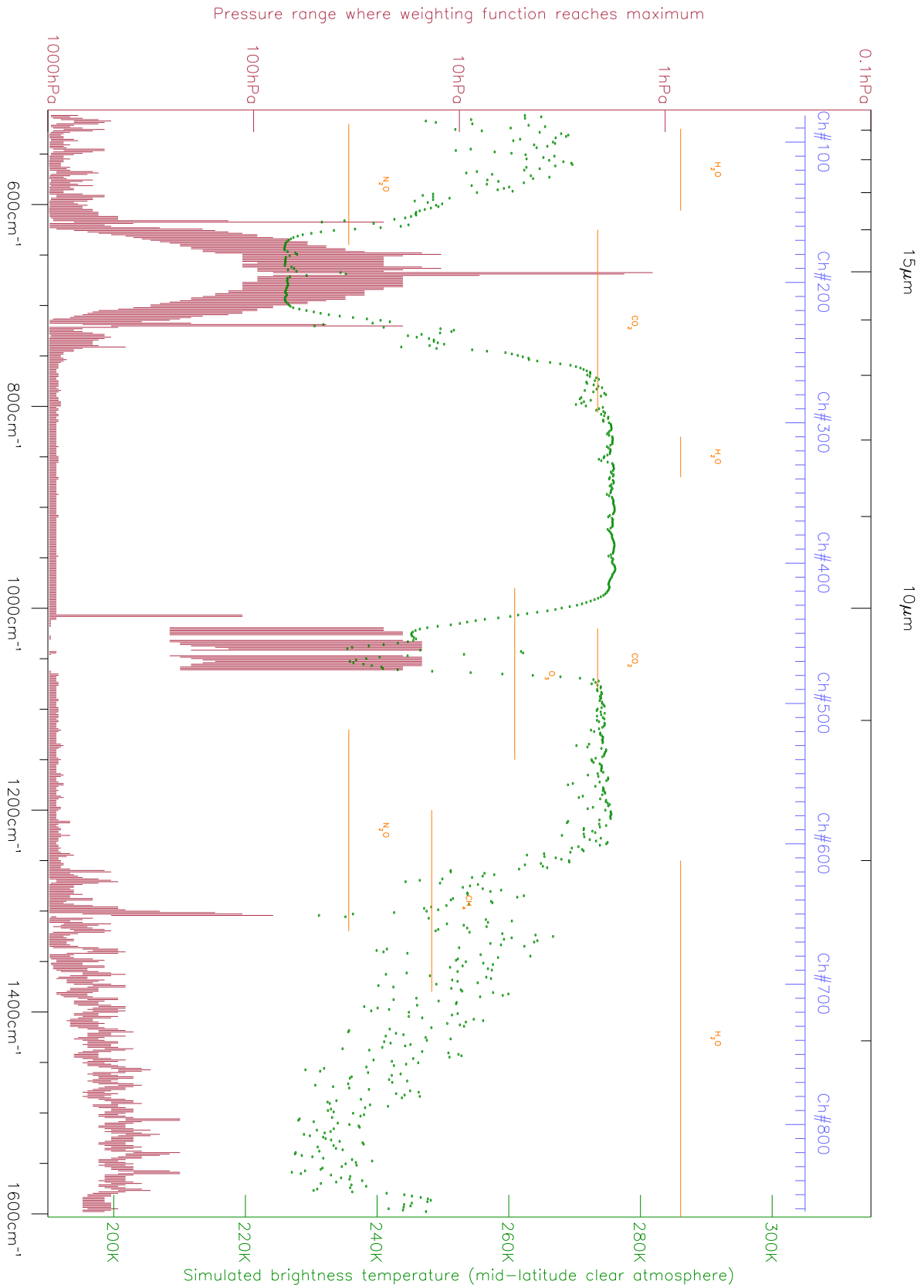
Figure 16: Simulated spectrum of brightness temperature (right vertical axis) for a mid-latitude profile, and pressure range where the weighting function reaches maximum values (left vertical axis), for Nimbus-IV IRIS channels 81 to 862.
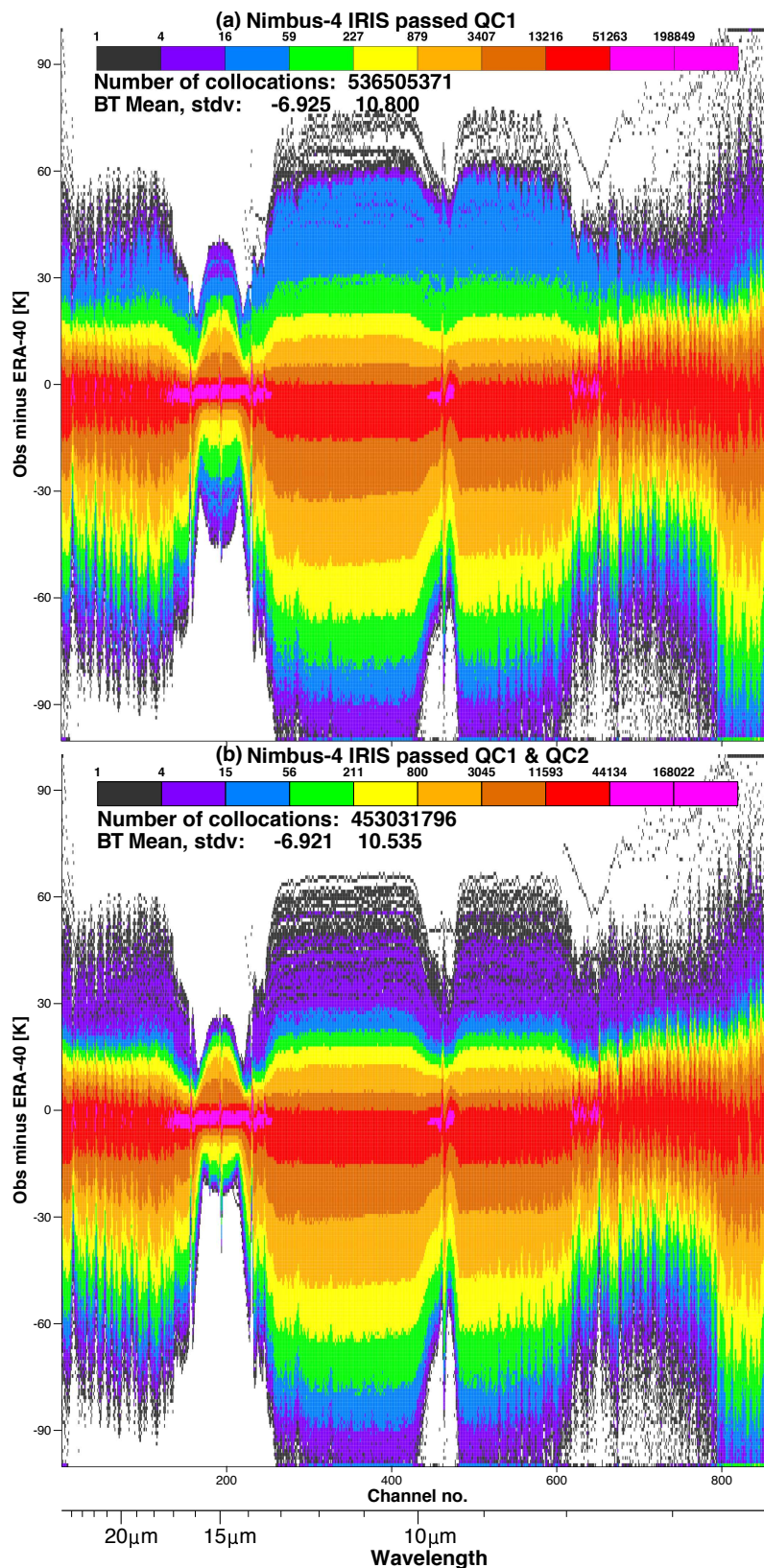
Figure 17: Density plot of observed brightness temperatures minus RTTOV calculations from ERA-40 for all spectra that passed (a) QC1 and (b) QC1 and QC2.
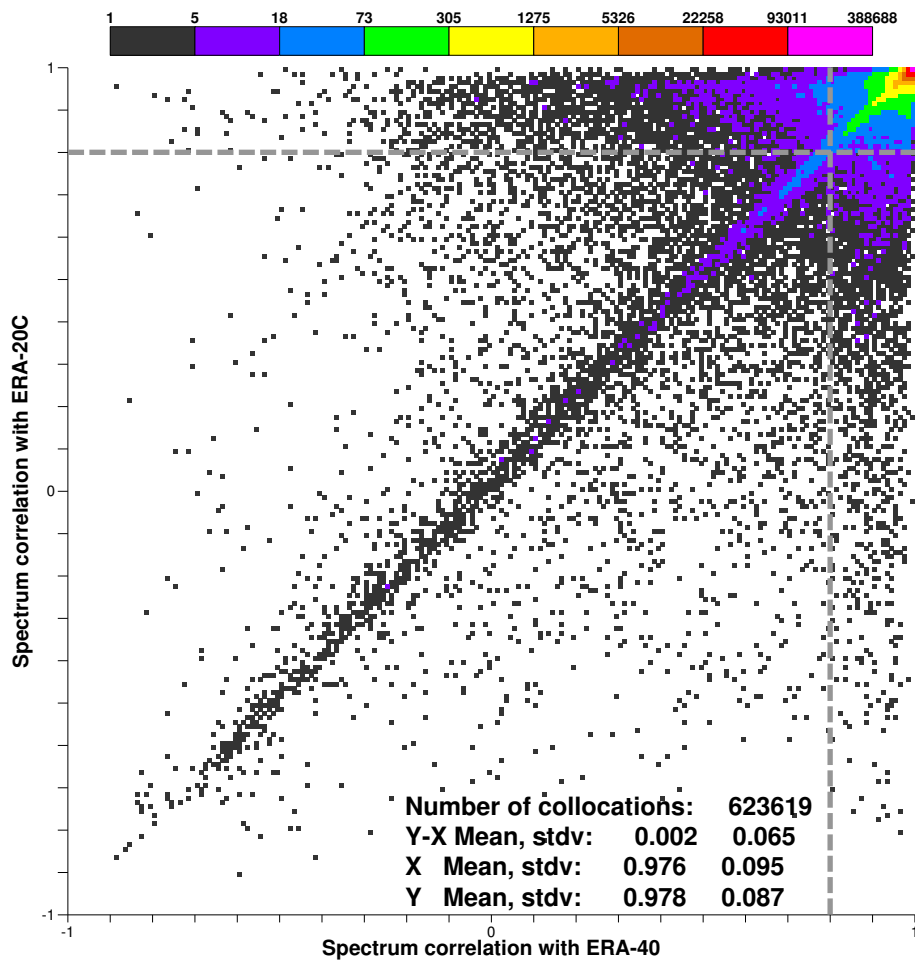
Figure 18: Density plot of correlations (on a per-spectrum basis) between observations and ERA-40 (horizontal axis) and between observations and ERA-20C simulations (vertical axis). The gray dotted lines indicate 0.8 correlation (r).
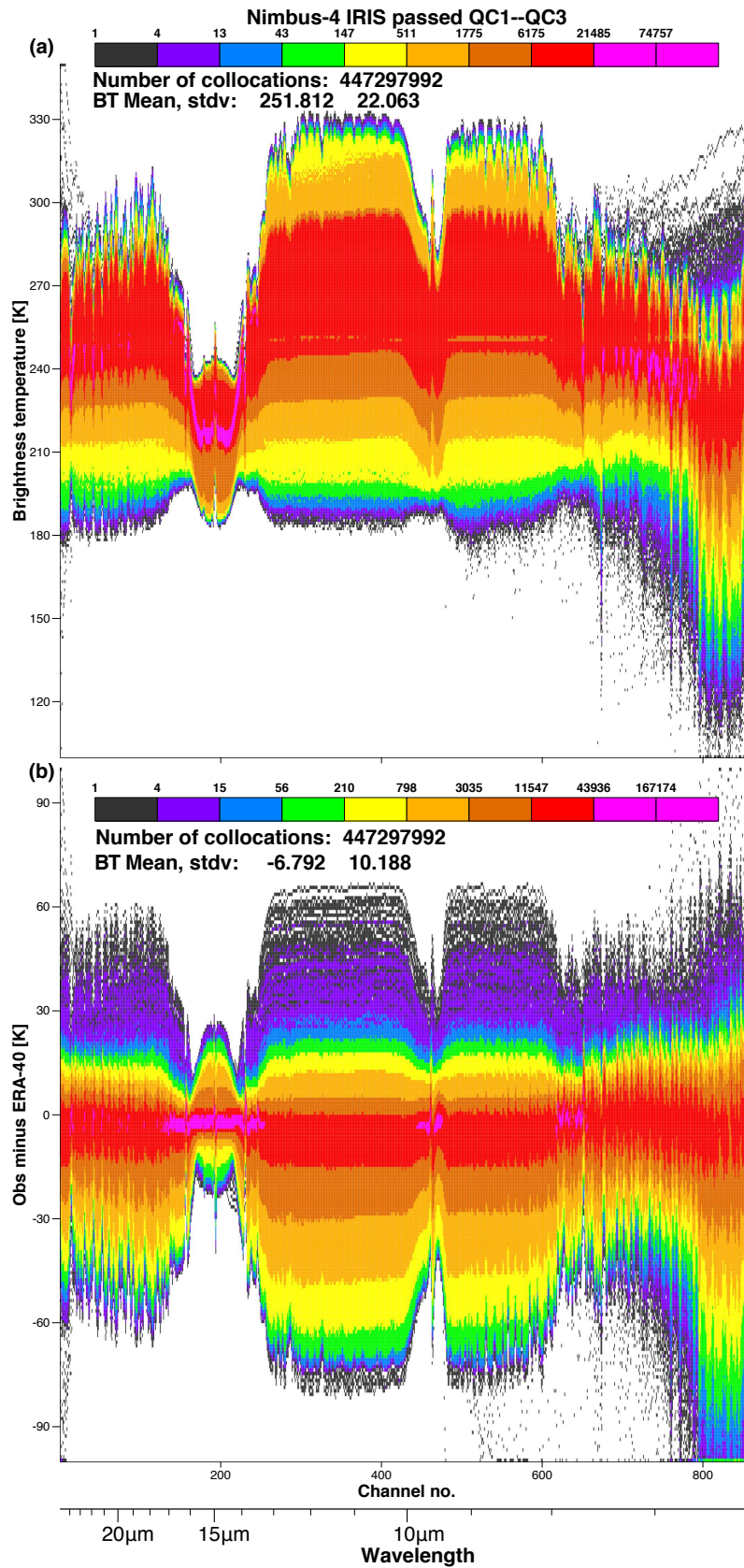
Figure 19: Density plot of (a) observed brightness temperatures passing QC1 to QC3 and (b) differences observations minus ERA-40 for the same data.

approach of McNally and Watts (2003). Channels are first ranked in the vertical, according to their height assignments. We then apply the scheme to process departures of the observations from brightness temperatures simulated by ERA-40 (and also to ERA-20C, we hence obtain two cloud detection estimates). For this study the cloud detection code is modified to handle the IRIS instrument. The following settings are employed. Only one spectral band is used for cloud detection: channels 145–290 (Figure 16 shows that this choice covers the P/Q/R branches of the 15 μm band). The cloud detection results from that band are applied to all IRIS channels according to their ranking in the vertical. The vertical ranking method is using exactly the same algorithm as in the ECMWF Integrated Forecasting System (IFS). After some experimentation, the following variables are used: N__GradChkInterval=5, N__Window_Width=20, N__Window_Bounds=0, R__BT_Threshold=2.5, R__Grad_Threshold=0.02, R__Window_Grad_Threshold=0.4, the so-called 'quick exit' is activated, but there is no use of imager-based cloud detection or aerosol detection.

The first aspect to be checked is that the cloud detection algorithm yields clear areas in line with current knowledge of clear versus cloudy areas on Earth. Figure 20 shows the prior probability of clear-sky at 1 km resolution from the Along-Track Scanning Radiometer (ATSR) on European Remote Sensing (ERS) satellites, by the ATSR Reprocessing for Climate (ARC) project. From IRIS, the results are shown in Figure 21. Note that IRIS features a much bigger pixel size, so we expect on average lower fractions of clear sky, which is indeed what we observe. Also, the correspondence between the clear areas in ATSR and IRIS are striking: Mediterranean Sea, South tropical Pacific, South tropical Atlantic, Mozambique channel, coast of Namibia, Eastern coast of Australia. These results are not a firm validation, but rather encouraging. However, we cannot know at this stage whether the clear sky statistics are any valid over the ice-covered regions such as Antarctica. There are several reasons why the cloud detection could fail there. One reason is that a cloud signature could resemble an incorrect surface temperature (Joiner et al., 2004). Another reason is that the algorithm employs ordering of channels by transmittance, and the results may be more sensitive in the case of an isothermal atmosphere (such situations can occur during the polar night).

Figure 22 shows the differences between IRIS and ERA-40 after application of this algorithm, using ERA-40 departures as input in the cloud detection. Departures in the window region are now more clustered around 0.0, though seemingly with a negative bias. This bias is more visible in Figure 23a. This plot considers all scenes, including those over land and sea-ice. Figure 24 restricts to scenes only over ocean, discarding land and sea-ice. The bias with respect to ERA-40 and ERA-20C is about -1 K in the window region, with standard deviations reaching below 1 K for some of the temperature sounding channels. Over oceans, the standard deviations appear smaller but the biases larger, suggesting either reanalysis biases or residual marine clouds that could not be removed.

For the data that passed all preceding QCs and cloud detection, the percentage of variance explained by reanalyses in the observations is another way to assess the level of realism in simulating the observations from the reanalyses. Figure 25 shows the proportion of variance in observations (believed to be cloud-free) explained by reanalysis simulations. This proportion is slightly higher for ERA-20C in the Tropics than for ERA-40 for the highest channels, suggesting that the stratosphere is probably better represented in the former than the latter (thanks to improvements between generations of IFS model versions). For channels peaking in the troposphere, Figure 26 shows that as one gets closer to the surface the explained variance increases more over land than ocean. In 1970, this may be caused by better analyzed conditions in the reanalysis over land (coinciding with a greater density of in situ observations) than over ocean. One way to reconcile this with the lower standard deviations of departures over ocean as compared to land is if the variabilities differ. Overall, the differences noted in behavior between ocean and land require more investigations.
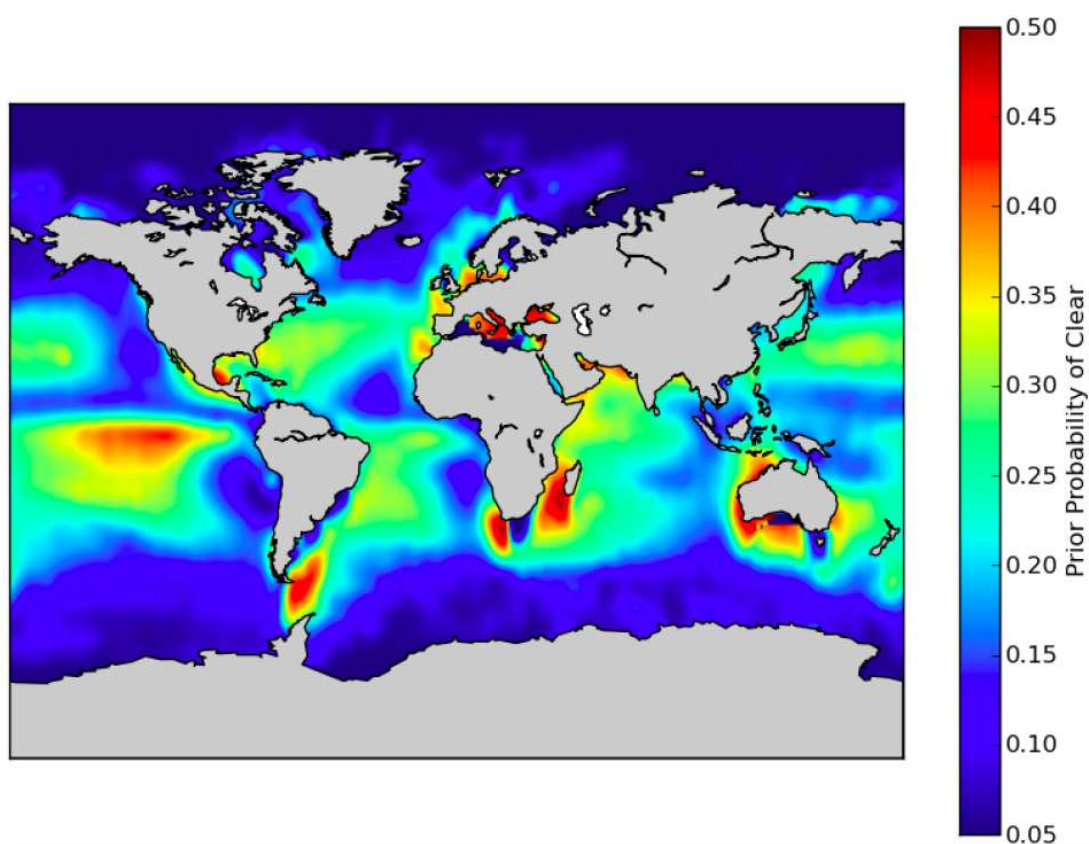
Figure 20: Map of the prior probability of clear-sky at 1 km resolution generated from ARC processing of ATSR data (source: EUMETSAT Bayesian Cloud Detection Algorithm Theoretical Basis Document Figure 4.3; Pearson et al., 2014)
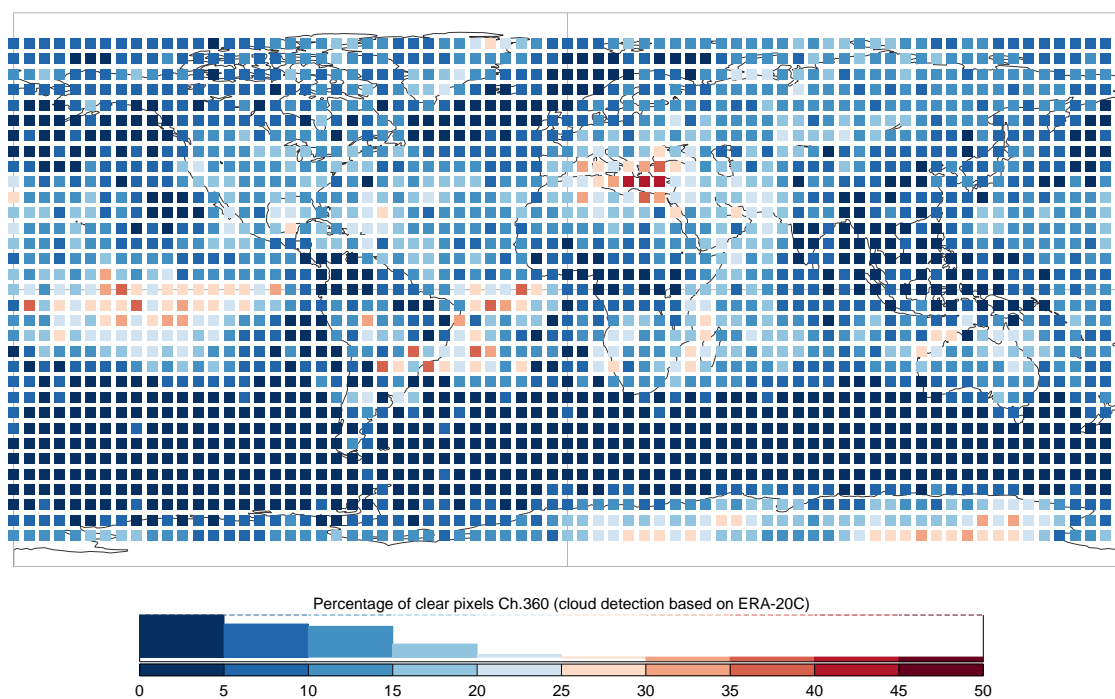
Percentage of clear pixels Ch.360 (cloud detection based on ERA-20C)

Figure 21: Map of percentage of clear pixels for Nimbus-IV IRIS window channel number 360 according to ERA-20C cloud detection.
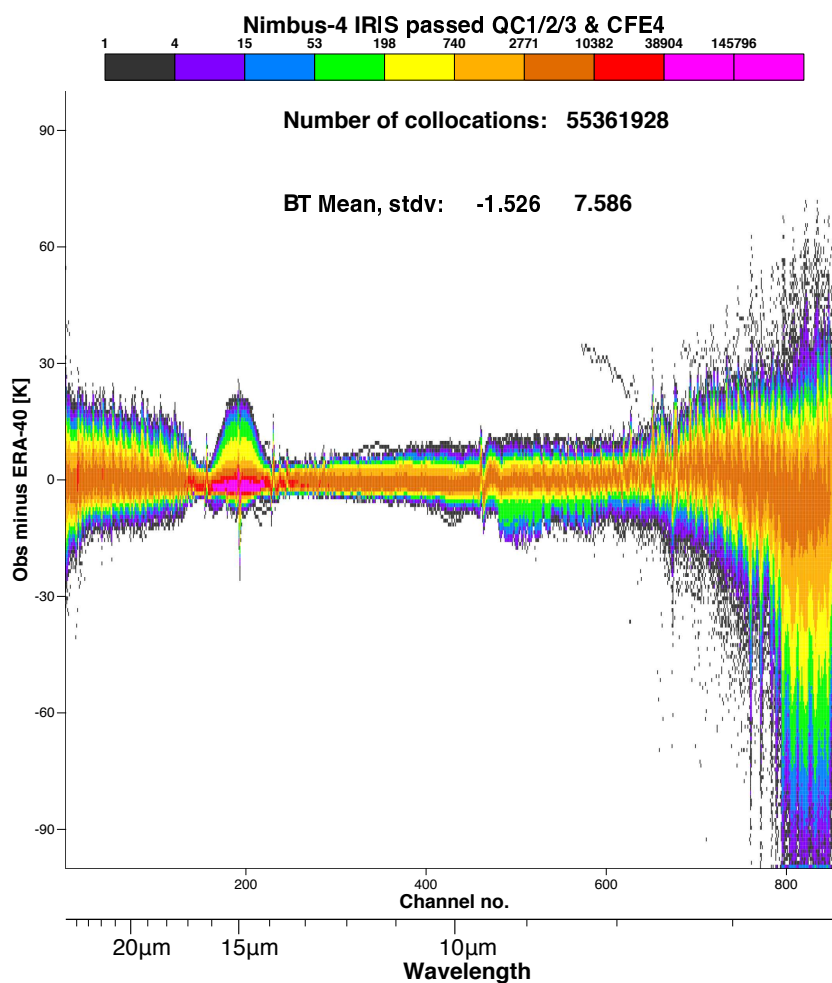
Figure 22: Density plot of differences observations minus ERA-40 using ERA-40-based cloud detection.

Nimbus-4 IRIS clear channels All scenes
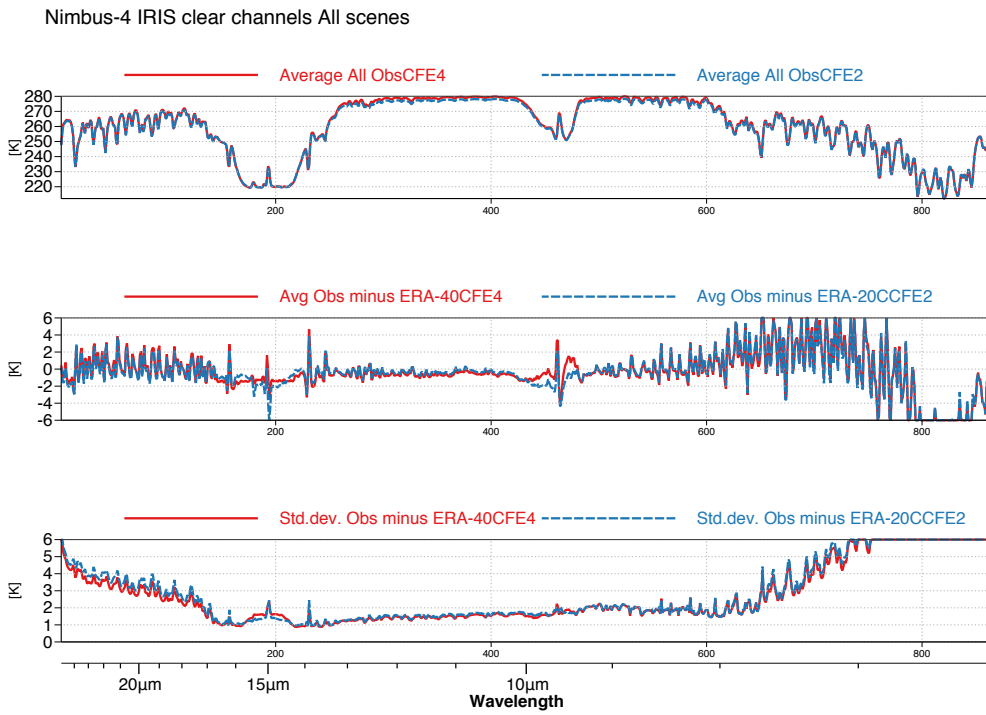
Figure 23: IRIS observations that passed cloud detection (top) mean observed values, (middle) mean differences with reanalyses, (bottom) standard deviation of differences with reanalyses.
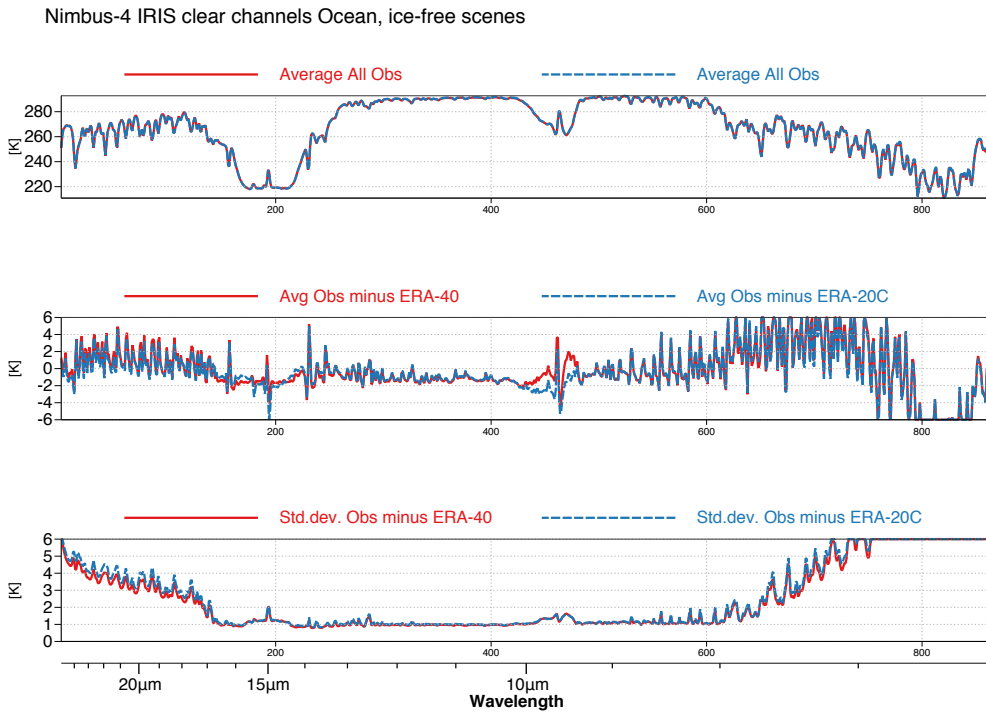
Nimbus-4 IRIS clear channels Ocean, ice-free scenes
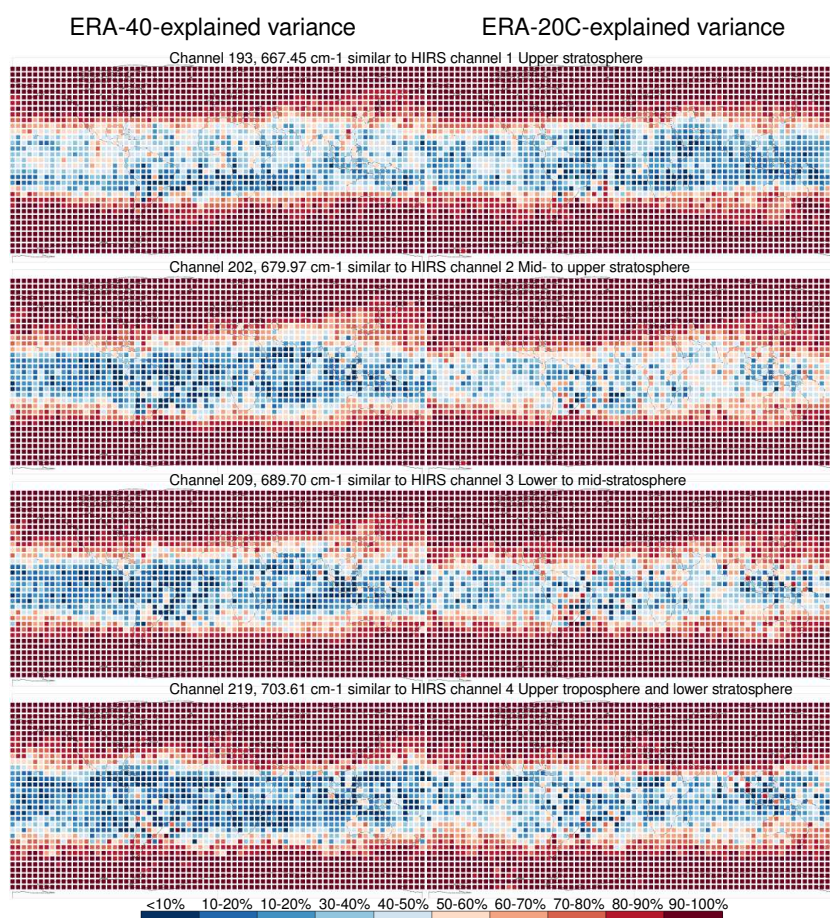

Figure 24: Same as Figure 23, but only over ocean and sea-ice-free scenes.

Figure 25: Left (right): percentage of ERA-40-explained (ERA-20C-explained) variance in observations. Explained variance is defined as 100 times the square of the correlation between observations and the RTTOV simulations from ERA-40 (ERA-20C, respectively). Four channels are shown here, all in the 15 μm band, peaking from the upper stratosphere to the upper troposphere, lower stratosphere.

ERA-40-explained variance   ERA-20C-explained variance
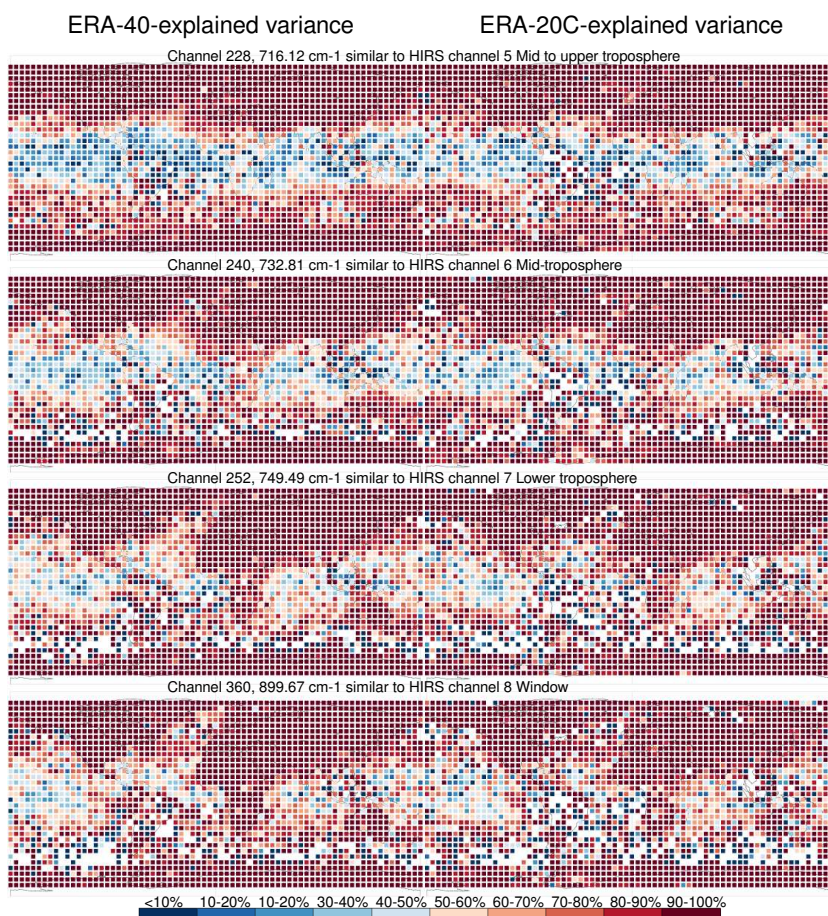

Figure 26: Same as Figure 25, but for a selection of channels peaking from the upper troposphere, lower stratosphere to the surface.

5   First in a long series, Nimbus-VI HIRS

When IRIS was planned, its scientific objectives did not include providing observations for operational numerical weather prediction. The data from such an interferometer was considered too large in volume and too detailed, and more suited for state-of-the-art research, to better understand atmospheric radiation and details of the spectra or dedicated meteorological studies. Generally, the goal pursued was the provision of spectra with the best accuracy possible, even if that meant compromising on the quantity of spectra, for example not using scanning by only collecting spectra at nadir. In fact, this initial intent is very similar to 18th century in situ measurements of air pressure, air temperature, and water temperature from ships; these were meant to improve the general pool of knowledge of the different types of weathers and where they occurred to improve navigation for future voyages. The goal was not really to reconstruct the global weather on those days.

Instead of IRIS, discrete filter radiometers or grating spectrometers were devised to collect a large number of soundings as required for use in numerical weather prediction, in addition to radiosoundings. On Nimbus-III and -IV, such was the role of the Satellite Infrared Spectrometer (SIRS), a 14-channel grating spectrometer. The instrument consisted of a much reduced number of channels as compared to IRIS, but was able to scan across track, and was thus considered suitable for the derivation of atmospheric profiles in large numbers, which would then feed into the process of analyzing the weather for numerical prediction. The 14 channels consisted of 7 channels in the 15 μm carbon dioxide (nu2 vibrational mode at 667 cm^{-1}), 1 channel in the window region at 899 cm^{-1}, and 6 channels in the water vapor rotational band.

The two SIRS instruments were followed by a more evolved instrument for operational applications, the Infrared Temperature Profile Radiometer (ITPR) on Nimbus-V, featuring higher horizontal resolution (about 32km at nadir instead of about 220 km previously), and improved cross-track scanning specifications (14 fields-of-view instead of 6 previously). However, the Principal Investigator of the mission himself indicates that this instrument suffered from a scan mirror problem and the usefulness of the data may be very limited (Bill Smith, personnal communication, 2011). The ITPR data mostly correspond to nadir-viewing, and may still be of use to propagate backward calibration information from current hyperspectral sounders, and confront it with calibration propagated forward from IRIS.

The next instrument to try discrete filters for infrared sounding in the Nimbus series was the High Resolution Infrared Radiometer (HIRS) on Nimbus-VI. This instrument was the first in a long series. Second-, third-, and fourth-generation HIRS/2, /3, and /4 instruments were mounted respectively on: TIROS-N (launched in 1979), NOAA-6 to -14; NOAA-15 to -17; NOAA-18 and -19 and MetOp-A and -B. Some of these instruments (the more recent ones) are still operating at the time of writing. The instrument on Nimbus-VI featured 42 fields-of-view across-track, a horizontal resolution around 25 km at nadir, and 17 channels (Landsat/Nimbus project, 1975). There is more than 30 years of accumulated knowledge on how to use HIRS data at NWP centers. However, the Nimbus-VI HIRS data have been the subject of very little study since the advent of HIRS/2, and Nimbus-VI HIRS have never been used in reanalyses.

For all these reasons, the Nimbus-VI HIRS data were identified as important at the beginning of the ERA-CLIM projects by Saunders et al. (2011), to enable to extend the reanalysis record backwards. After notifying strong interest in the recovery of these data, they were rescued from ageing tapes by NASA GES DISC in 2014. This is the dataset that is used in the following section.

5.1   Raw dataset

Data pre-processing for this study is as described in the previous section for IRIS. First, the data are read from their native format by a program created from sample code provided by NASA GES DISC. In a second step,
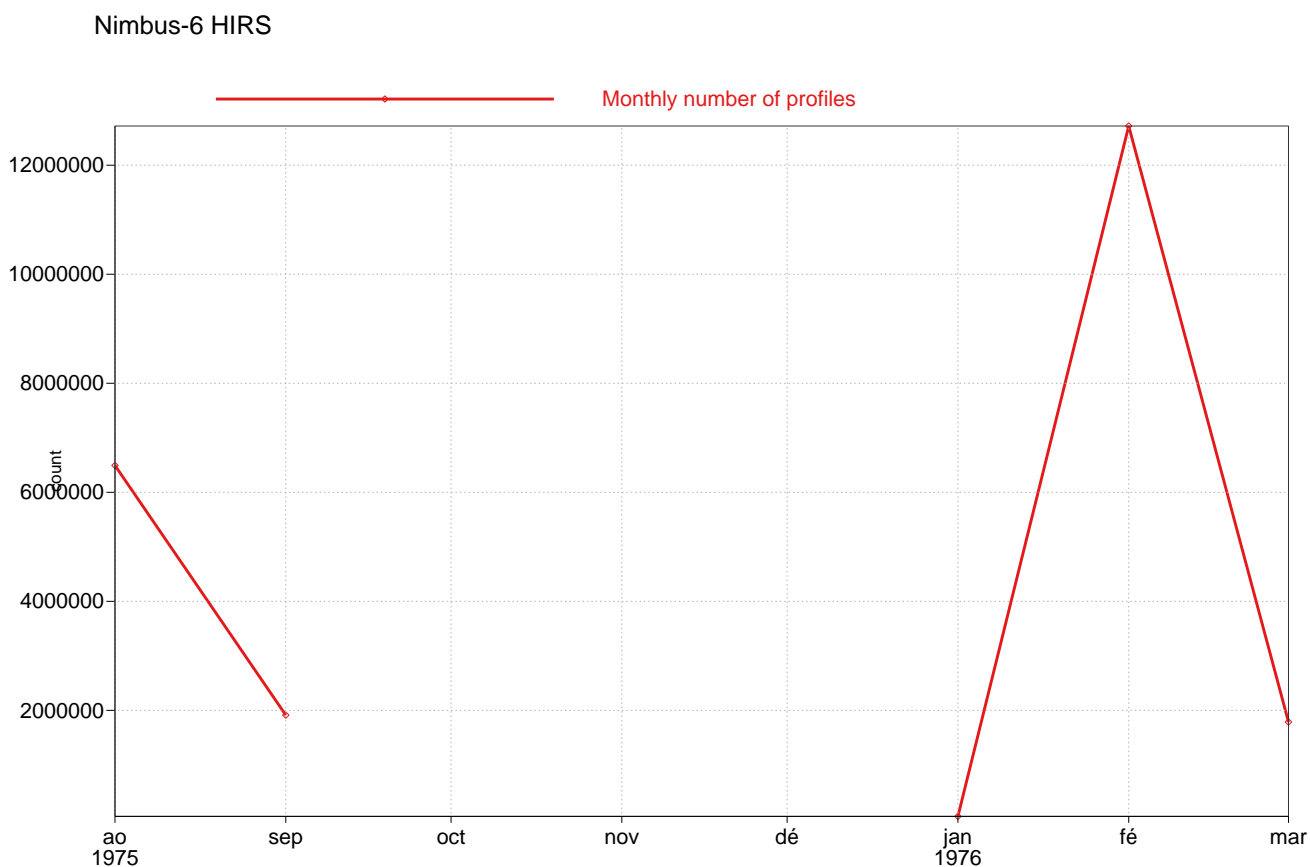
Nimbus-6 HIRS

Figure 27: Monthly count of Nimbus-VI HIRS 17-channel spectra

the resulting data are written into ODB format.

Figure 27 shows the monthly data count of spectra. The dates covered are 17 August to 4 September 1975 and 31 January to 4 March 1976. There are many more spectra than for IRIS because each scan covers 42 fields-of-view. Binning the data by location, Figure 28 shows the complete coverage achieved by the Nimbus-VI HIRS experiment.

5.2   Simple quality controls

The 17 channels are described in the user's guide (Landsat/Nimbus project, 1975). Briefly, the first 7 channels Figure 29 shows daily maps of calibrated radiances for the window channel (number 8) found in the dataset, after applying QC1 devised earlier. The geolocation appears correct at the 5 degree x 5 degree horizontal resolution employed for the maps. Cloud formations are visible.

Showing channel 5 (716 cm^{-1}), sensitive to the mid- to upper-troposphere, indicates in Figure 30 that for a few dates there are erroneous swaths of data, essentially at the end of both sensing periods available. Removing these dates forms the second quality control step.
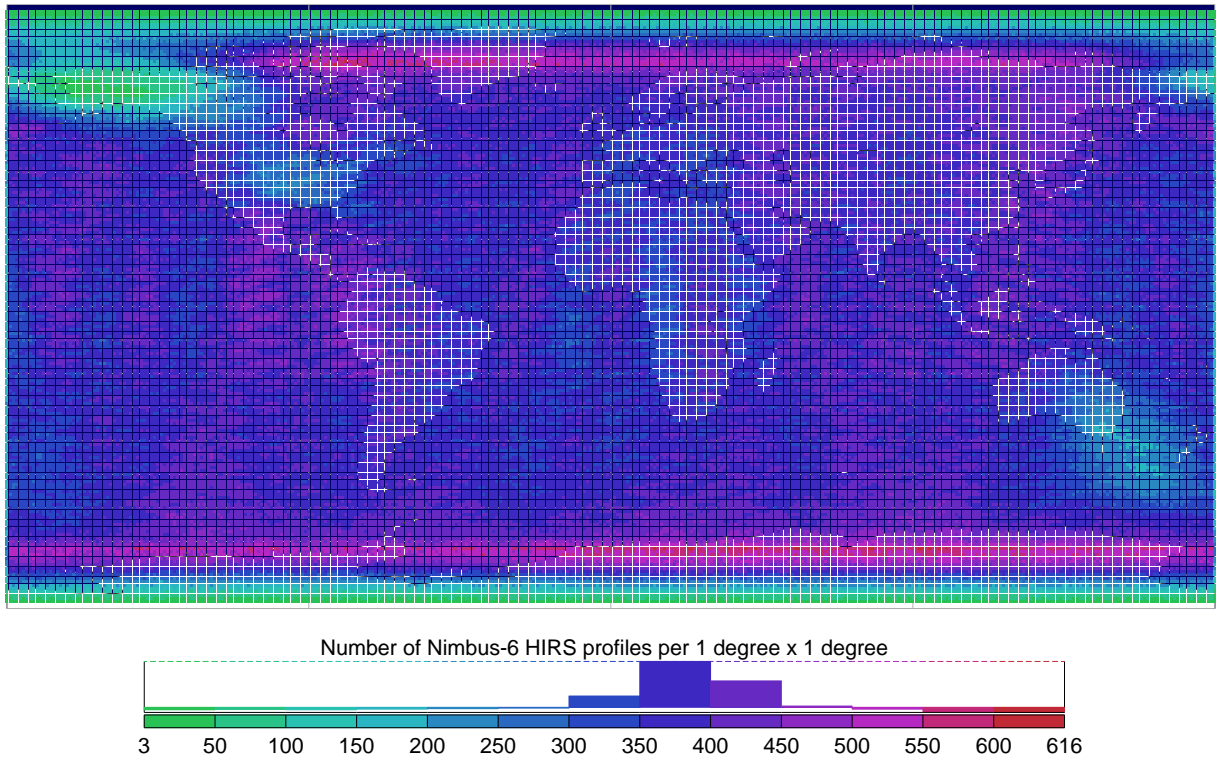
Number of Nimbus-6 HIRS profiles per 1 degree x 1 degree

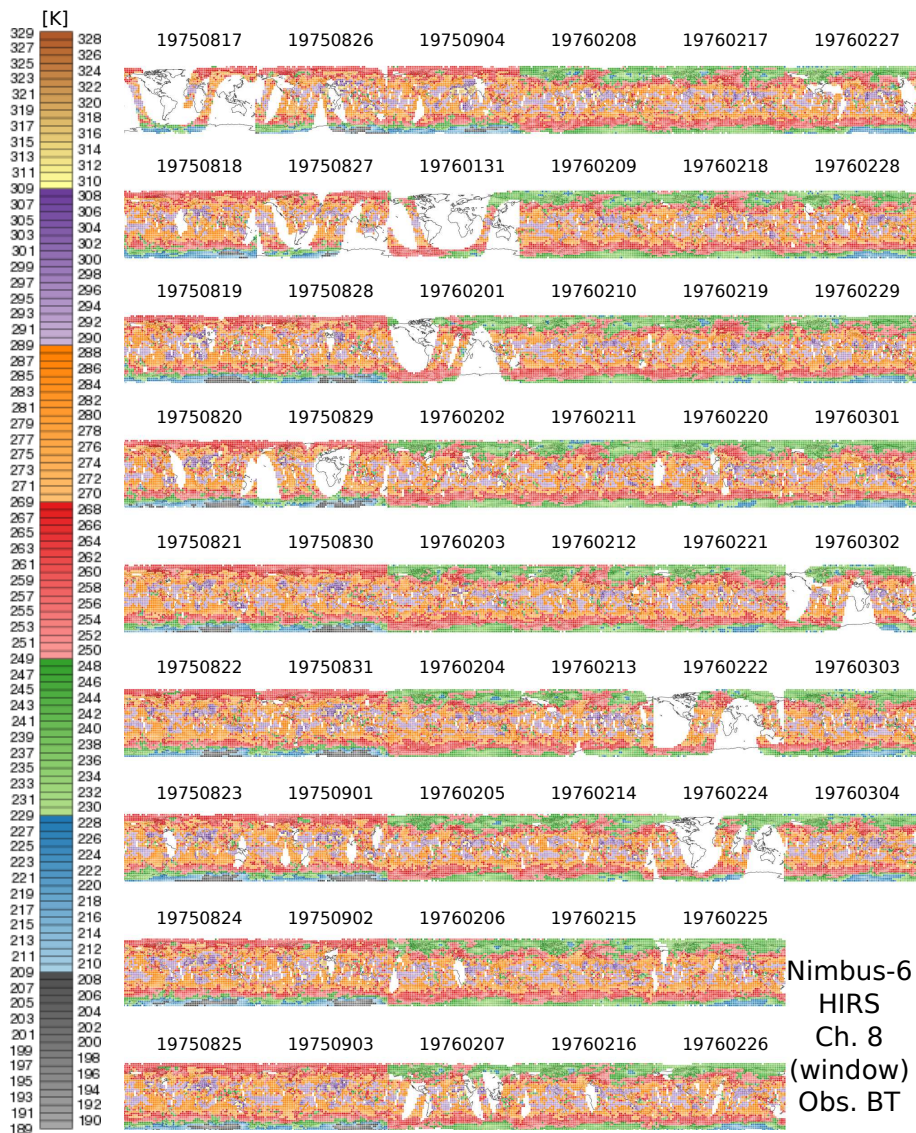*Figure 28: Map of count of Nimbus-VI HIRS soundings*

Figure 29: Daily maps of channel 8 calibrated radiance observations found in the Nimbus-VI HIRS dataset, passing QC1.
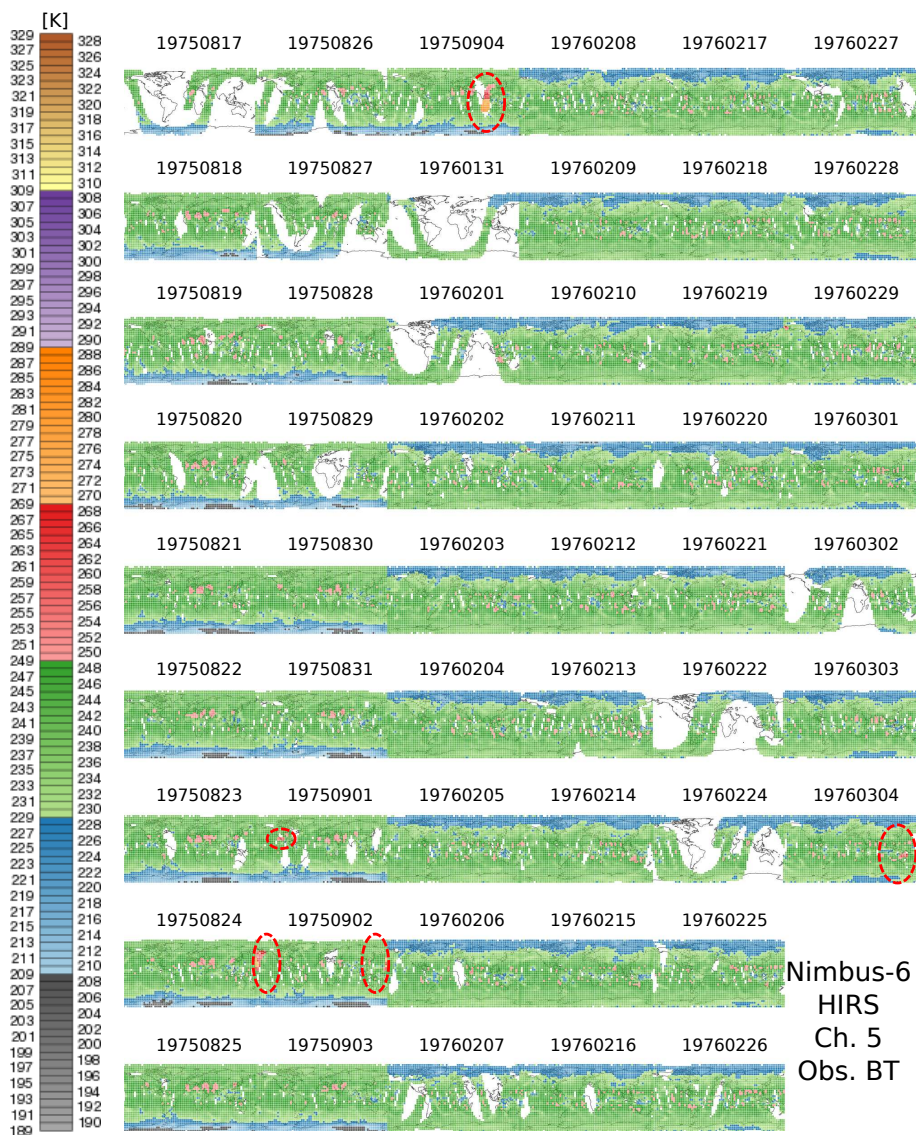
Figure 30: Same as Figure 29, but for channel 5.

6 Comparison of Nimbus-VI HIRS with atmospheric reanalyses

Using the same method as described earlier for IRIS, clear-sky radiative transfer calculations (RTTOV) are applied to the ERA-20C reanalysis fields to simulate Nimbus-VI HIRS.

6.1 Prior RTTOV preparations

The version of RTTOV used here is RTTOV v11.1. The Nimbus-VI HIRS ISRF is a pre-requisite for any radiative transfer simulations. This function is used to convolve line-by-line calculations for transmittances or radiances. The HIRS instrument on board Nimbus-VI was build in 1971-1974 by the International Telephone and Telegraph (ITT) Aerospace/Optical Division (Fort Wayne, Indiana) under NASA contract NAS-5-21651. This HIRS instrument was the first of several generations, and is hence called HIRS/1 in the remainder of this section to avoid confusion with later generations of that instrument (HIRS/2 to /4). Unfortunately we did not find a readily available copy of the HIRS/1 ISRF data. However, Ronald Glumb (Harris/Exelis, former ITT) found in 2013 the original HIRS/1 calibration book. From there a scan of the filter spectral performance plots was provided, matching the specific filters that went into HIRS/1. Indeed, the filters that went onto Nimbus-VI were selected at the time among the prototype filters, the flight model 1 filters, and the flight model 2 filters. The quality of the document received was good enough for digitisation. After conversion of that document to raster images with sufficient resolution, a digitization software produced usable ISRF data for RTTOV coefficient generation. For example, Figure 31 shows the summary sheet for instrument that was eventually launched. The first column indicates the origin of the filter (prototype, or flight model 1, or flight model 2). The second column shows the centre frequency. The half-bandwidth is indicated in the third column. This number hides great complexity. For example, for channel 8, the ISRF is far from a parametric curve, as shown by Figure 32, which explains why the ISRFs had to be scanned individually.

Nimbus-VI HIRS was followed by TIROS-N HIRS. The two instruments feature quite similar ISRFs for all channels, except for Nimbus-VI channel 16 (3.7 μm) which is much broader than TIROS-N. Note that there are 3 more channels for TIROS-N HIRS, which is the first of second-generation HIRS or HIRS/2. The 3 channels are located approximately at 10 μm, 7.3 μm, and 4.0 μm. Figure 33 shows that, for the channels common to all, Nimbus-VI HIRS instrument was very close to the following generation HIRS/2 onboard TIROS-N (instrument of this generation flew until NOAA-14).

The ISRF for Nimbus-VI HIRS have been used for RTTOV coefficient generation. These coefficients are now available from the NWP-SAF (`https://nwpsaf.eu/`).

6.2 RTTOV application

The radiative transfer calculations allow to explore the field-of-view dependence of the departures from observations. Figure 34 indicates that modeling channel 1 presents serious issues. Channels 2, 3, and 4 appear unaffected by clouds, but with no dependence to the field-of-view . However, the comparisons for channels 3 and 4 suggest a few cases where observations are abnormally larger than the background (note the very small density of points in this situation). Channels 5 to 8 are increasingly subject to clouds, and the modes of departures remain centered close to zero, as expected. The first water vapor channel (channel 9) presents also cloud contamination. The second water vapor channel (channel 10) has problems of scenes with abnormally large departures, like channel 11. The temperature sounding channels in the second band present a specific problem of unexplained, non-symmetric dependence to the scanning.

The large, abnormal departures would be screened out by the quality controls of assimilation in IFS. The next

TABLE 5.1-1   BANDPASS/SPECTRAL DATA SUMMARY SHEET (Protoflight)

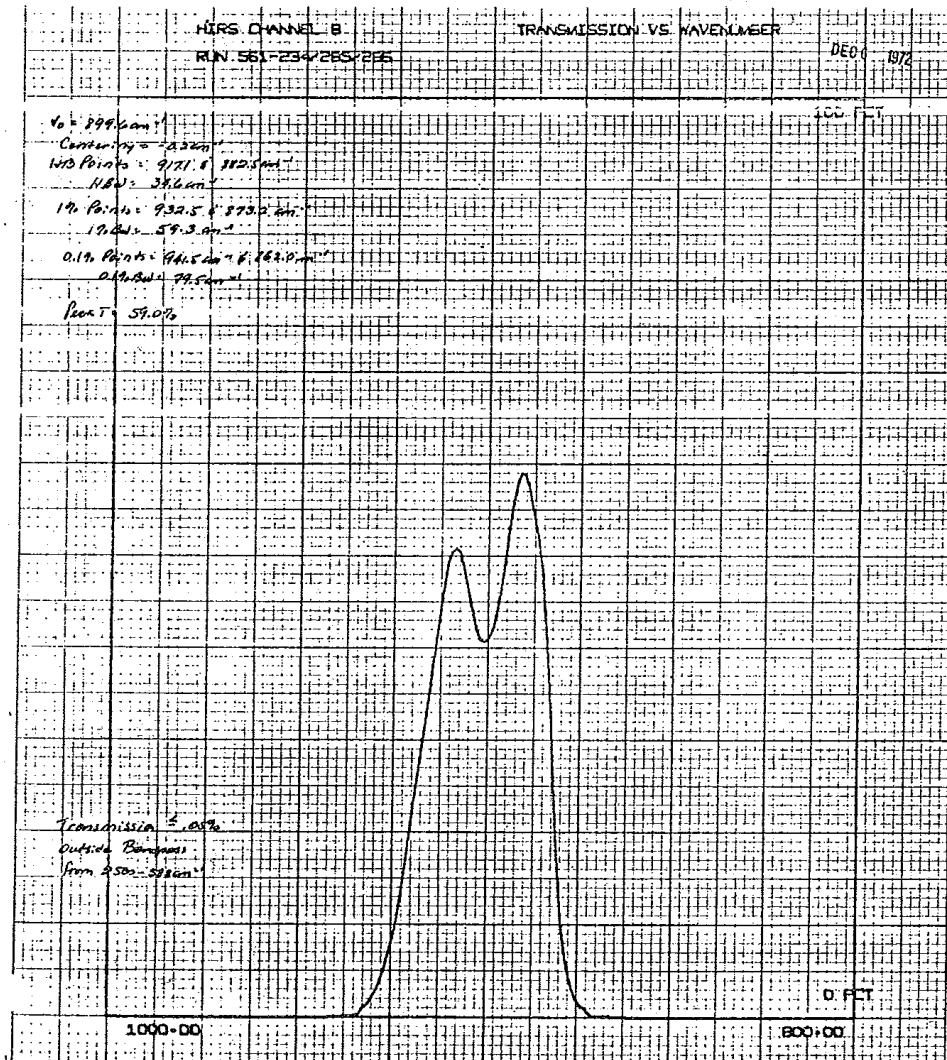| Filter Channel Set		CM-1 Center Freq.	CM-1 Half Bandwidth	CM-1 Effective Bandwidth	CM-1 1.0%T-ABS Bandwidth	CM-1 0.1%-ABS Bandwidth	Peak Transmission	CM-1 HBW Centering	Uniformity	Leaks	Temperature Shift *
1	Proto	669.1	2.8	4.2	17.3	30.6	37.6%	-0.1	OK	2400-588 OK	OK
2	Flight-2	678.8	13.7	13.6	26.3	37.2	59.9	0	OK	2350-588 OK	OK
3	Proto.	690.1	12.6	12.3	28.0	41.2	64.7	-0.2	OK	2350-588 OK	OK
4	Flight-1	701.6	15.9	16.1	36.8	52.8	70.3	+0.2	OK	2300-588 OK	OK
5	Flight-1	716.5	17.5	18.1	37.4	55.7	63.3	+0.1	OK	2500-588 OK	OK
6	Flight-1	732.3	17.6	17.9	39.2	59.4	63.7	-0.2	OK	2500-588 OK	OK
7	Proto.	749.1	18.4	19.3	38.6	60.2	58.2	0	OK	2500-588 OK	OK
8	Flight-2	899.6	34.6	31.7	59.3	79.5	59.0	-0.2	OK	2500-588 OK	OK
9	Flight-1	1228.2	63.4	57.1	90.5	111.1	70.3	-2.7	OK	2500-588 OK	OK
10.	Flight-2	1494.9	87.6	79.4	150.4	192.1	68.7	+0.2	OK	2500-588 OK	OK
11	Flight-1	2190.8	20.6	20.7	44.7	67.3	54.7	+0.4	OK	6250-1755 OK	OK
12	Proto.	2211.9	22.5	23.0	46.7	71.1	60.7	-0.3	OK	6250-1755 OK	OK
13	Flight-1	2244.2	21.6	21.6	41.0	62.4	53.7	+0.3	OK	6250-1755 OK	OK
14	Flight-1	2274.5	35.2	35.0	75.5	121.0	54.3	+0.6	OK	6250-1755 OK	OK
15	Flight-1	2357.6	23.0	23.0	46.8	73.0	68.4	+0.1	OK	6250-1755 OK	OK
16	Proto	2692.4	296.9	203.5	474.9	707.1	89.0	-3.4	OK	6250-1755 OK	OK
17	Proto.	14,443	892.2	N/A	N/A	N/A	88.3	N/A	OK	OK	N/A

5-8

Figure 31: Summary table for the channels of the Nimbus-VI HIRS. (reproduced from NASA document (Koenig, 1975), page 107)

Figure 32: Instrument spectral response function for Nimbus-VI HIRS channel 8. Source: ITT, document produced under NASA contract NAS-5-21651
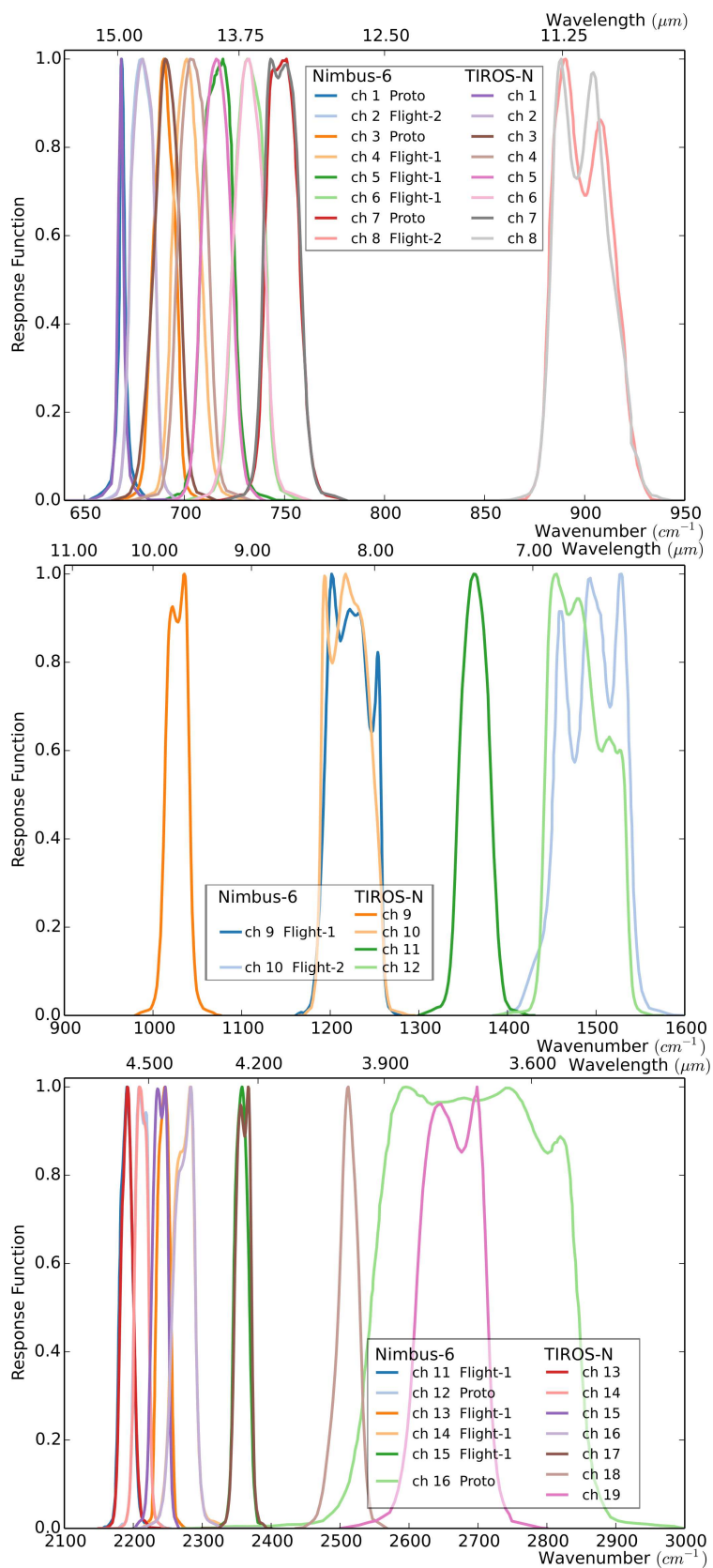
Figure 33: Instrument spectral response function for Nimbus-VI and TIROS-N HIRS instruments. Top (bottom) horizontal axes show wavelengths (wavenumbers).
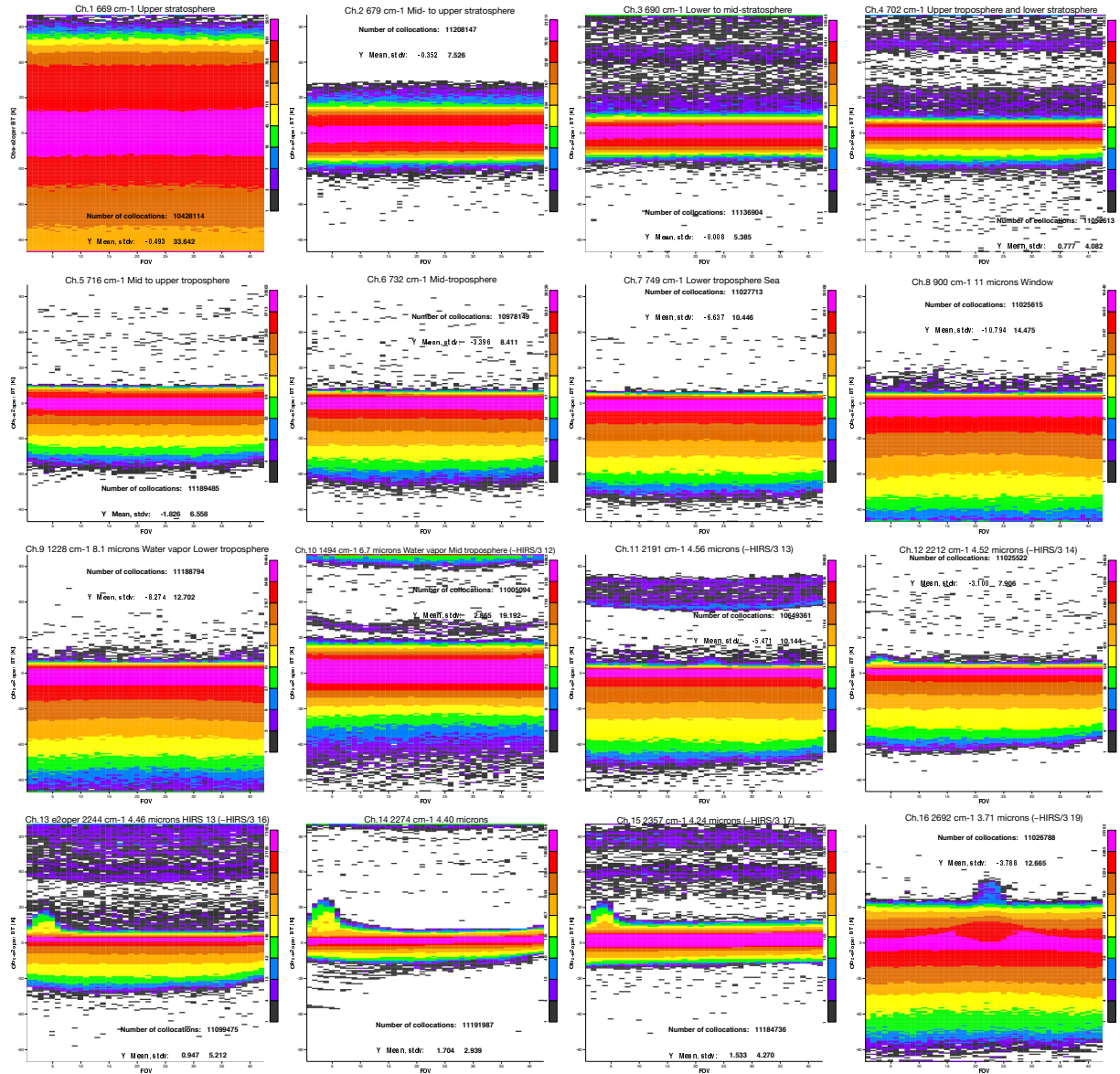
Figure 34: Field-of-view (horizontal axis) dependence of observation minus ERA-20C departures (vertical axis), for scenes over ocean and believed to be sea-ice-free (according to ERA-20C). Each entry in the panel shows a different channel. Nimbus-VI HIRS data are filtered to only retain those that passed the quality controls described in the earlier section.

step for the evaluation of this sensor would be to apply a cloud detection. However, this is optimally done for a such a low (spectral) resolution sounder in the assimilation, with the assistance of the most accurate background possible. Consequently, the next suggested step for evaluation is to test the assimilation, given that the methodology is generally already in place in the IFS for other HIRS instruments. Note the cloud detection method used for IRIS cannot be used for low spectral resolution instruments such as HIRS. The assimilation will also prove whether the scheme for variational bias correction is able to correct for the few scan-dependent effects seen in this section.

7 Conclusions and future work

The present report considers two historical sets of meteorological observations from satellites and compares them with state-of-the-art models and reanalyses. An essential ingredient in this comparison is the fast radiative transfer model RTTOV, which benefited from several upgrades between the time this effort was initiated and the final version of this report.

The IRIS observations from April 1970 to January 1971 and the HIRS observations from August 1975 to March 1976 are too short to extend the reanalysis record backwards, *e.g., via* direct assimilation. However, by their quality, the IRIS observations could help as a benchmark to pinpoint and attribute biases in reanalyses and their underlying forcings (SST, sea-ice). Should the low-resolution spectral infrared sounder data on the same Nimbus-IV satellite be recovered as well (from SIRS), this would open the prospect of calibrating the latter with the former (Wang *et al.*, 2007), using simultaneous nadir overpass (SNO) comparisons. Using SNO, one could then propagate forward these corrections from one sounder to the next (ITPR, VTPR, HIRS). Eventually, if the SSH data from DMSP were recovered and if one could make use of the pressure-modulated radiometers (SCR and PMR) and broadband imagers such as THIR, one would be able to connect the entire line of infra-red sounders to TIROS-N, and from there, the present times. Then, doing the same backwards, starting from IASI and CrIS, one would be able to propagate current, state-of-the-art corrections, such as derived by GSICS, to Nimbus-IV SIRS and IRIS. Overall, this double check would allow to provide a quantified estimate of uncertainty in the cumulated chain of inter-calibrations and help better qualify the trends in derived products. The Nimbus-VI HIRS observations are hence important to achieve such line of satellite inter-calibration. Such findings would then directly feed into the following reanalyses and improve climate research.

This initial effort summarized here produced quality-controlled datasets of observations augmented with feed-back, archived on ECMWF MARS infrastructure. The final results indicate standard deviations of comparisons of IRIS to reanalyses within 1 K for some of the temperature channels, but a bias over ocean around -1 K (observations being colder than simulations). At the time of writing, the cause for this bias is unknown, but we know of several limitations in our present work. First, the actual concentrations for several trace gases used for training the fast radiative transfer model do not match the levels of 1970. Second, the cloud detection assumes unbiased differences with simulations in input, and could benefit from using collocated imager data. Third, the actual wavelengths measured by IRIS may vary from the values found in all published documentation; a small offset in wavenumber would indeed generate a constant bias.

Before using the Nimbus-IV IRIS observations to possibly assess the biases in reanalyses, all these issues must be addressed. The following tasks are recommended as follow-up: (1) extend the mechanism to train the fast radiative transfer model to cover the admissible range of all relevant trace gases to the 1970 levels; (2) use the Nimbus-IV Temperature-Humidity Infrared Radiometer (THIR) observations in the 11.5 μm channel (available from NASA GES DISC) to improve the cloud detection, and (3) assess if offsets in the central wavenumbers would reduce the residual biases with respect to the reanalysis simulations. Another point to consider would be to use a greater diversity of reanalyses (with differing models, forcings, and observation data input), such as

JRA-55 (Kobayashi *et al.*, 2015) or NOAA/ESRL 20CR (Compo *et al.*, 2011).

Regarding Nimbus-VI HIRS, the brightness temperature data appear to be ready for assimilation, when compared to ERA-20C. However, the record currently available is quite short, amounting to less than 6 months of data. Efforts must continue to locate more radiance data from that sounder.

Acknowledgement

References

Bartman FL. 1968. Quarterly report of ORA project 05863 High Altitude Radiation Measurements, University of Michigan College of Engineering, High Altitude Engineering Lab. http://deepblue.lib.umich.edu/bitstream/handle/2027.42/3445/bab0791.0001.001.txt

Bengtsson L, Shukla J. 1988. Integration of Space and In Situ Observations to Study Global Climate Change. Bull. Amer. Meteor. Soc. 69, 1130-1143

Chaney LW, Drayson SR, Young C. 1967. Fourier transform spectrometer - Radiative measurements and temperature inversion. App. Opt. 6 (2):347-349. doi:10.1364/AO.6.0347_1

Christy JR, Norris WB, Spencer RW, Hnilo JJ. 2007. Tropospheric temperature change since 1979 from tropical radiosonde and satellite measurements. J. Geophys. Res. 112: D06102. doi:10.1029/2005JD006881

Clough SA, Shephard MW, Mlawer EJ, Delamere JS, Iacono MJ, Cady-Pereira K, Boukabara S, Brown PD. 2005. Atmospheric radiative transfer modeling: a summary of the AER codes. Short Communication, J. Quant. Spectrosc. Radiat. Transfer, 91:233-244

Compo GP, Whitaker JS, Sardeshmukh PD, Matsui N, Allan RJ, Yin X, Gleason BE, Vose RS, Rutledge G, Bessemoulin P, Brönnimann S, Brunet M, Crouthamel RI, Grant AN, Groisman PY, Jones PD, Kruk MC, Kruger AC, Marshall GJ, Maugeri M, Mok HY, Nordli O, Ross TF, Trigo RM, Wang XL, Woodruff SD, Worley SJ. 2011. The Twentieth Century Reanalysis Project. Q.J.R. Meteorol. Soc., 137: 1–28. DOI: 10.1002/qj.776

Connes J. 1958. Domaine d'utilisation de la mthode par transformee de Fourier. J. Phys. Radium, 19, 197-208, doi:10.1051/jphysrad:01958001903019700

Dee DP, Uppala S. 2009. Variational bias correction of satellite radiance data in the ERA-Interim reanalysis. Quart. J. R. Meteorol. Soc., 135, 1830-1841

Eresmaa R. 2015. ECMWF Aerosol and Cloud Detection Software, User Guide 1.2. 15 pp. ECMWF, Reading,

United Kingdom. Document and software available from the NWP-SAF at
https://nwpsaf.eu/deliverables/IR_aerosol_cloud_detect/

Gregow H, Jylhä K, Mäkelä HM, Aalto J, Manninen T, Karlsson P, Kaiser-Weiss AK, Kaspar F, Poli P, Tan DGH, Obregon A, Su Z. 2015. Worldwide survey of awareness and needs concerning reanalyses, and respondents views on climate services. Bull. Amer. Meteorol. Soc. DOI:10.1175/BAMS-D-14-00271.1

Hanel RA, Schlachman B, Rogers D, Vanous D. 1970. The Nimbus-4 Michelson interferometer. NASA Tech. Memo. X-65395. NASA Goddard Space Flight Center, Greenbelt, Maryland, USA

Joiner J, Poli P, Frank D, Liu HC. 2004. Detection of cloud-affected AIRS channels using an adjacent-pixel approach. Q.J.R. Meteorol. Soc. 130:1469-1487. DOI:10.1256/qj.03.93

Kobayashi S, Ota Y, Harada Y, Ebita A, Moriya M, Onoda H, Onogi K, Kamahori H, Kobayashi C, Endo H, Miyaoka K, Takahashi K. 2015. The JRA-55 reanalysis: General specifications and basic characteristics. J. Meteor. Soc. Japan. 93: DOI:10.2151/jmsj.2015-001

Koenig, EW. 1975. High Resolution Infrared Radiation Sounder (HIRS) for the Nimbus F Spacecraft. NASA-CR-144743, NASA Goddard Space Flight Center, Greenbelt, Maryland, available from http://ntrs.nasa.gov/search.jsp?R=19760014184 (last accessed 7 February 2016)

Kuchta. P. 2009. Observation feedback archiving in MARS. 12th Workshop on Meteorological Operational Systems, 2-6 November 2009. ECMWF, Reading, United Kingdom.
http://www.ecmwf.int/newsevents/meetings/workshops/2009/MOS_12/Presentations/Kuchta.pdf

Kunkee, DB, Poe GA, Boucher DJ, Swadley SD, Hong Y, Wessel JE, Uliana EA. 2008. Design and evaluation of the first Special Sensor Microwave Imager/Sounder. IEEE Trans. Geosci. Remote Sens. 46:4. DOI:10.1109/TGRS.2008.917980

Landsat/Nimbus project. 1975. Nimbus VI user's guide. Edited by JE Sissala. Last accessed 7 January 2016 from http://acdisc.gsfc.nasa.gov/data/s4pa/Nimbus6_THIR_Level2/THIRN6IM.001/doc/NimbusVIUG.pdf

Lu Q, Bell W. 2014. Characterising channel center frequencies in AMSU-A and MSU microwave sounding instruments. J. Atmos. Ocean. Tech., doi: http://dx.doi.org/10.1175/JTECH-D-13-00136.1

McNally AP, Watts PD. 2003. A cloud detection algorithm for high-spectral resolution infrared sounders. Quart. J. R. Meteorol. Soc., 129 (595): 3411-3423, doi:10.1256/qj.02.208

McPeters RD, Bhartia PK, Haffner D, Labow GJ, Flynn L. 2013. The version 8.6 SBUV ozone data record: An overview. J. Geophys. Res. Atmos., 118, 8032-8039, doi:10.1002/jgrd.50597

Michelson AA, Morley EW. 1887. On the relative motion of the Earth and the luminiferous ether. Am. J. Science 34: 333-345

Murcray DG, Murcray FH, Williams WJ. 1962. Distribution of water vapor in the stratosphere as determined from infrared absorption measurements. J. Geophys. Res. 67 (2): 759-766, doi:10.1029/JZ067i002p00759

NASA. 2014. Nimbus program history, with foreword by R Shapiro (Nimbus Operations Manager 1963-1980). Access on 12 March 2014 from http://atmospheres.gsfc.nasa.gov/uploads/files/Nimbus_History.pdf

Nimbus project. 1970. Nimbus IV user's guide. Edited by RR Sabatini. Last accessed 12 March 2014 from http://ntrs.nasa.gov/archive/nasa/casi.ntrs.nasa.gov/19730014076_1973014076.pdf

Pearson K, Embury O, Bulgin C. 2014. Bayesian Cloud Detection Algorithm Theoretical Basis Document. EUM-BC-ATBD-003, available from EUMETSAT
http://www.eumetsat.int/website/home/Data/TechnicalDocuments/index.html Last

accessed 25 December 2015

Poli P, Hersbach H, Berrisford P, Dee D, Simmons A, Laloyaux P. 2015. ERA-20C Deterministic. 53 pp. ECMWF, Reading, United Kingdom. Last accessed 24 December 2015 from http://www.ecmwf.int/sites/default/files/elibrary/2015/11700-era-20c-deterministic.pdf

Reichhardt T. 2006. The first photo from space. Smithsonian Air and Space Magazine. http://www.airspacemag.com/space/the-first-photo-from-space-13721411/

Saunders R, Poli P, John V, Kelly G. 2011. Satellite Datasets for use in ERACLIM. 8 pp. ERA-CLIM project deliverable. Available from ECMWF, Shinfield Park, RG2 9AX Reading, United Kingdom

Saunders R, Hocking J, Rundle D, Rayer P, Matricardi M, Geer A, Lupu C, Brunel P, Vidot J. 2013. RTTOV-11 science and validation report. EUMETSAT NWP SAF, 62pp. Available at http://nwpsaf.eu/deliverables/rtm/rtm_rttov11.html

Simmons AJ, Poli P, Dee DP, Berrisford P, Hersbach H, Kobayashi S, Peubey C. 2014. Estimating low-frequency variability and trends in atmospheric temperature using ERA-Interim. Q.J.R. Meteorol. Soc.. doi: 10.1002/qj.2317

Uppala SM, and Co-authors. 2005. The ERA-40 re-analysis. Q.J.R. Meteorol. Soc., 131: 2961-3012. doi: 10.1256/qj.04.176

Van Allen JA. 1958. Observation of High Intensity Radiation by Satellites 1958 Alpha and Gamma, Journal of Jet Propulsion, 28(9):588–592. DOI: 10.2514/8.7396

Wang L, Cao C, Ciren P. 2007. Assessing NOAA-16 HIRS Radiance Accuracy Using Simultaneous Nadir Overpass Observations from AIRS. J. Atmos. Oceanic Technol., 24, 1546-1561. doi:10.1175/JTECH2073.1

Appendix A: Description of the dataset archived on the ECMWF Observation Feedback Archive (OFA)

The Nimbus-IV IRIS data used in this study have been archived on ECMWF Observation Feedback Archive (OFA). This archive is built on ECMWF Meteorological Archiving and Retrieval System (MARS). The Nimbus-IV IRIS data, as well as quality controls and supplemental data computed from ERA-40 and ERA-20C, are now available for researchers worldwide via a web interface. The present section describes the data format and contents.

The archiving format is ECMWF Observation DataBase (ODB), a flat format which uses compression and is suitable to process large batches of observations. An ODB decoder is available to users, and can be found at the same place where the data are accessible for download. The data can also be retrieved in text format.

The data are arranged as a two-dimensional matrix: each row constitutes a single data record that contains a fixed number of columns, documented in Table 2.

Number	Name	Type	Description
Columns derived from the raw data, or for archive indexing and book-keeping			
1	andate@desc	Integer	Closest synoptic date (e.g. 19710103)
2	antime@desc	Integer	Closest synoptic time, in HHMMSS format (e.g. 60000 for 06UTC)
3	azimuth@sat	Real	Satellite azimuth angle, always missing
4	bt677outofbounds@qc	Integer	Quality control indicator, set to 1 if the brightness temperature at 677 cm^{-1} is outside the range 150–250 K (set to 0 if inside that range)
5	btflat@qc	Integer	Quality control indicator, set to 1 if the brightness temperature spectra are nearly flat (set to 0 if found to have some variability)
6	btnearlycst@qc	Integer	Quality control indicator, set to 1 if the brightness temperature spectra are supiciously flat (set to 0 if found to have sufficient variability)
7	bufrtype@hdr	Integer	BUFR type code (constant, set to 3)
8	class@desc	Integer	MARS archiving class (constant, set to 22)
9	cloudy_8minus11@qc	Integer	Quality control indicator, set to 1 if the observed brightness differences between 8 and 11 μm are larger than 8 K, suggesting possibly a cloudy scene (set to 0 if thought to be a clear scene according to that test)
10	codetype@hdr	Integer	IFS internal observation type (constant, set to 210)
11	date@hdr	Integer	Date of the observation, from the TAP files, in YYYYMMDD format (e.g. 1971010103)
12	entryno@body	Integer	Number of the record within the spectrum (ranges from 1 to 862)
13	expver@desc	String	MARS experiment version (constant, set to '1936 ')
14	groupid@hdr	Integer	MARS observation group code (constant, set to 47)
15	lat@hdr	Real	Latitude of the observation, in degrees (positive for the Northern hemisphere), from the TAP files (e.g. 8.729300)
16	lon@hdr	Real	Longitude of the observation, in degrees (positive towards the East), from the TAP files (e.g. 74.3936)

Table 2 – continued from previous page

Number	Name	Type	Description
17	obsradiance@body	Real	Observed radiance, from the TAP files, in W/m^2/ster/cm^1 (e.g., -2.201336 W/m^2/ster/cm^1)
18	obstype@hdr	Integer	IFS internal observation type code (constant, set to 7)
19	obsvalue@body	Real	Observed brightness temperature, converted from the radiance and the wavenumber, in K (e.g., 152.232101 K), missing if obsradiance@body¡0.0
20	orbit@radiance	Integer	Mission orbit number, from the TAP files (e.g. 3626)
21	reportype@hdr	Integer	MARS observation report type code (constant, set to 46002)
22	satellite_identifier@sat	Integer	WMO satellite identifier code (constant, set to 764), indicating Nimbus-IV
23	satellite_instrument@sat	Integer	WMO satellite instrument code (constant, set to 404), indicating IRIS
24	scanline@radiance	Integer	Scan number along the orbit, from the TAP files (e.g., 361)
25	scanpos@radiance	Integer	Scan position across-track, always missing since IRIS was only pointed at nadir
26	sensor@hdr	Integer	RTTOV sensor code (constant, set to 69), indicating IRIS
27	seqno@hdr	Integer	Number of the sounding within a 6-hour analysis window (e.g., 452)
28	source@hdr	String	Origin of the data (constant, set to 'NASAGSFC')
29	stalt@hdr	Real	Satellite altitude, always missing
30	stream@desc	Integer	MARS stream code (constant, set to 1025)
31	subtype@hdr	Integer	BUFR sub-type code (constant, set to 54)
32	surface_class@modsurf	Integer	Surface type, always missing
33	time@hdr	Integer	Observation time (UTC), from the TAP files, in HH-MMSS format (e.g., 70203 for 07:02:03 UTC)
34	type@desc	Integer	MARS type code (constant, set to 263)
35	varno@body	Integer	IFS geophysical variable code (constant, set to 119), indicating brightness temperature
36	vertco_reference_1@body	Real	Channel number (ranges from 1 to 862)
37	vertco_type@body	Integer	IFS vertical coordinate type (constant, set to 3), indicating that the data are organized by satellite channel number
38	wavelength@body	Real	Observation wavelength, in μm (ranges from 6.258955 to 24.970631)
39	wavenumber@body	Real	Observation wave number, from the TAP files (ranges from 400.470459 to 1597.710693)
40	zenith@sat	Real	Satellite zenith angle (constant, set to 0.0)

Columns derived from collocation with ERA-20C

Table 2 – continued from previous page

Number	Name	Type	Description
41	cloudy_1126@e2oper	Integer	Cloud detection flag from the channel at 1126 cm^{-1} and departures from ERA-20C, set to 1 if these departures exceed 6 K, indicating possibly a cloudy scene (set to 0 if thought to be a clear scene according to that test)
42	cloudy_917@e2oper	Integer	Cloud detection flag from the channel at 917 cm^{-1} and departures from ERA-20C, set to 1 if these departures exceed 6 K, indicating possibly a cloudy scene (set to 0 if thought to be a clear scene according to that test)
43	cloud_flag@e2oper	Integer	Cloud detection flag for the channel, set to 1 if a cloud is suspected, using McNally and Watts scheme
44	rank_cld@e2oper	Real	Channel height ranking for cloud detection (0.0 indicates top of atmosphere, 100.0 indicates surface)
45	emis@e2oper	Real	Emissivity computed by RTTOV from the ERA-20C atmospheric conditionse (e.g., 0.937489)
46	fg_depar@e2oper	Real	Difference in brightness temperatures, observation minus RTTOV computation from the ERA-20C atmospheric conditions, in K (e.g., 16.943197), can be missing if obsvalue@body is missing
47	fgradiance@e2oper	Real	RTTOV radiance computation from the ERA-20C atmospheric conditions, in W/m^2/ster/cm^1 (e.g., 1.423569 W/m^2/ster/cm^1)
48	fgvalue@e2oper	Real	RTTOV brightness temperature computation from the ERA-20C atmospheric conditions, in K (e.g., 213.709442)
49	lsm@e2oper	Real	Land-sea mask from ERA-20C (ranges from 0.0 for sea only to 1.0 for land only)
50	orography@e2oper	Real	Surface orography from ERA-20C, in meters (e.g., 3.895655)
51	seaice@e2oper	Real	Fraction of sea-ice from ERA-20C conditions (ranges from 0.0 for ice-free to 1.0 for 100% sea-ice coverage)
52	t2m@e2oper	Real	Two-meter temperature from ERA-20C conditions, in K (e.g., 298.114380)
53	tsfc@e2oper	Real	Skin temperature from ERA-20C conditions, in K (e.g., 300.708221)
54	u10m@e2oper	Real	Zonal component of the ten-meter wind wind from ERA-20C atmospheric conditions, in m/s (positive towards the East)
55	v10m@e2oper	Real	Meridional component of the ten-meter wind wind from ERA-20C atmospheric conditions, in m/s (positive towards the North)
Columns derived from collocation with ERA-40			
56	cloudy_1126@e4	Integer	Same as cloudy_1126@e2oper, but from ERA-40 instead of ERA-20C

Table 2 – continued from previous page

Number	Name	Type	Description
57	cloudy_917@e4	Integer	Same as cloudy_917@e2oper, but from ERA-40 instead of ERA-20C
58	cloud_flag@e4	Integer	Same as cloud_flag@e2oper, but from ERA-40 instead of ERA-20C
59	rank_cld@e4	Real	Same as rank_cld@e2oper, but from ERA-40 instead of ERA-20C
60	emis@e4	Real	Same as emis@e2oper, but from ERA-40 instead of ERA-20C
61	fg_depar@e4	Real	Same as fg_depar@e2oper, but from ERA-40 instead of ERA-20C
62	fgradiance@e4	Real	Same as fgradiance@e2oper, but from ERA-40 instead of ERA-20C
63	fgvalue@e4	Real	Same as fgvalue@e2oper, but from ERA-40 instead of ERA-20C
64	lsm@e4	Real	Same as lsm@e2oper, but from ERA-40 instead of ERA-20C
65	orography@e4	Real	Same as orography@e2oper, but from ERA-40 instead of ERA-20C
66	seaice@e4	Real	Same as seaice@e2oper, but from ERA-40 instead of ERA-20C
67	t2m@e4	Real	Same as t2m@e2oper, but from ERA-40 instead of ERA-20C
68	tsfc@e4	Real	Same as tsfc@e2oper, but from ERA-40 instead of ERA-20C
69	u10m@e4	Real	Same as u10m@e2oper, but from ERA-40 instead of ERA-20C
70	v10m@e4	Real	Same as v10m@e2oper, but from ERA-40 instead of ERA-20C

Table 2: List of columns in the Nimbus-IV IRIS dataset archived
at ECMWF

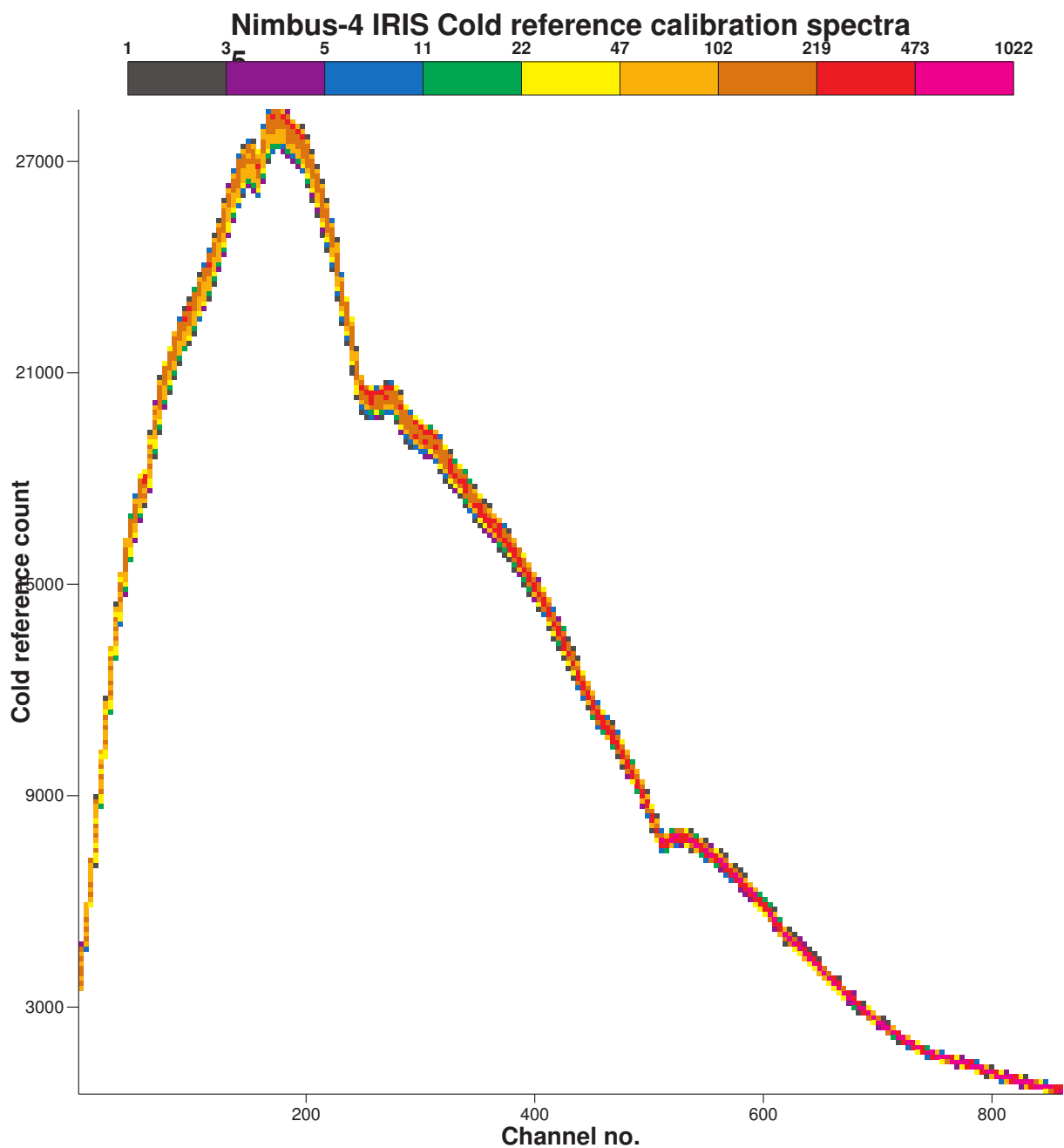**Appendix B: Additional IRIS instrument health status metadata spectra found in the IRIS dataset**

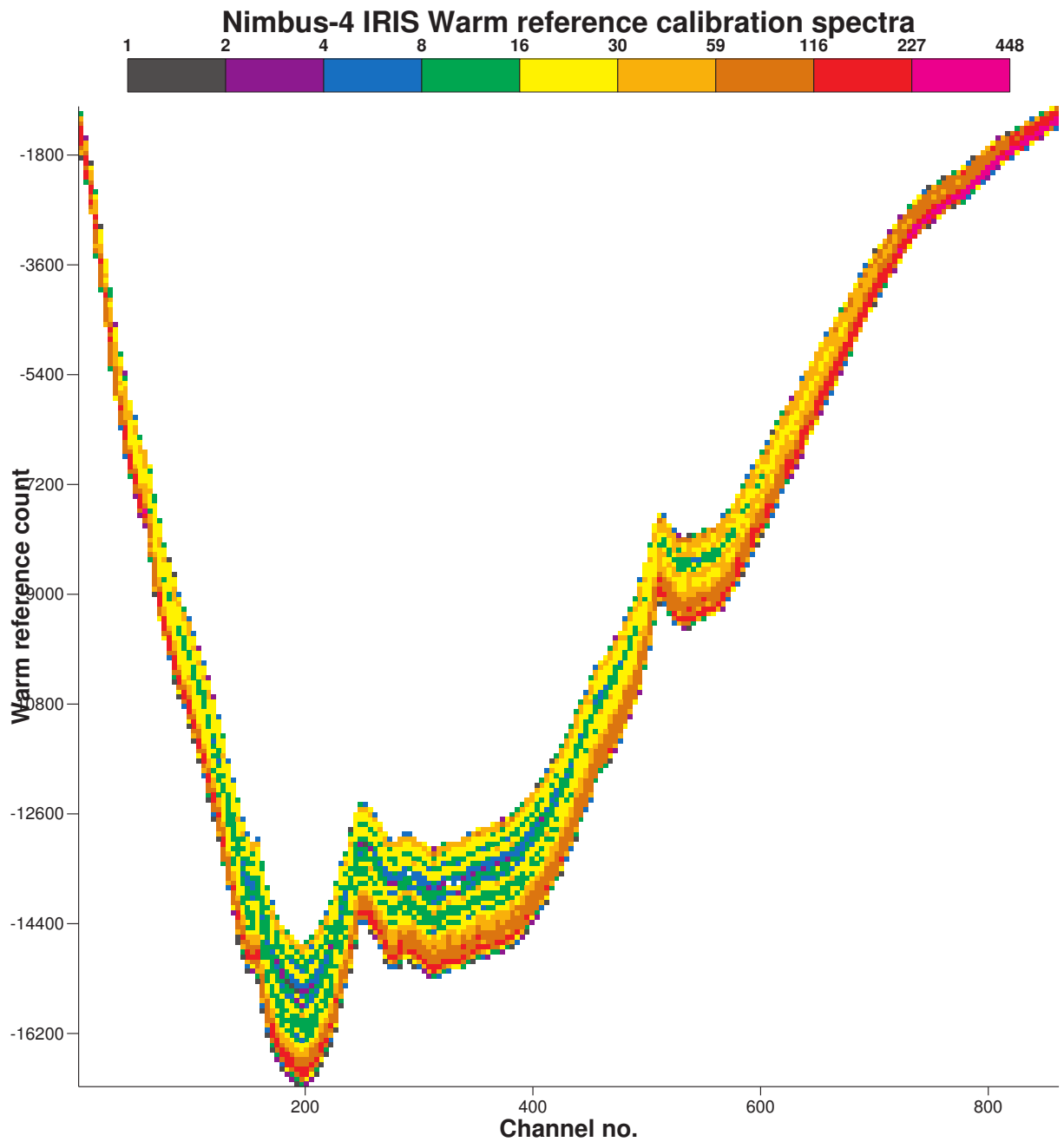*Figure 35: Cold calibration counts spectra (IRIS dataset record type 2)*

Figure 36: Warm calibration counts spectra (IRIS dataset record type 3)
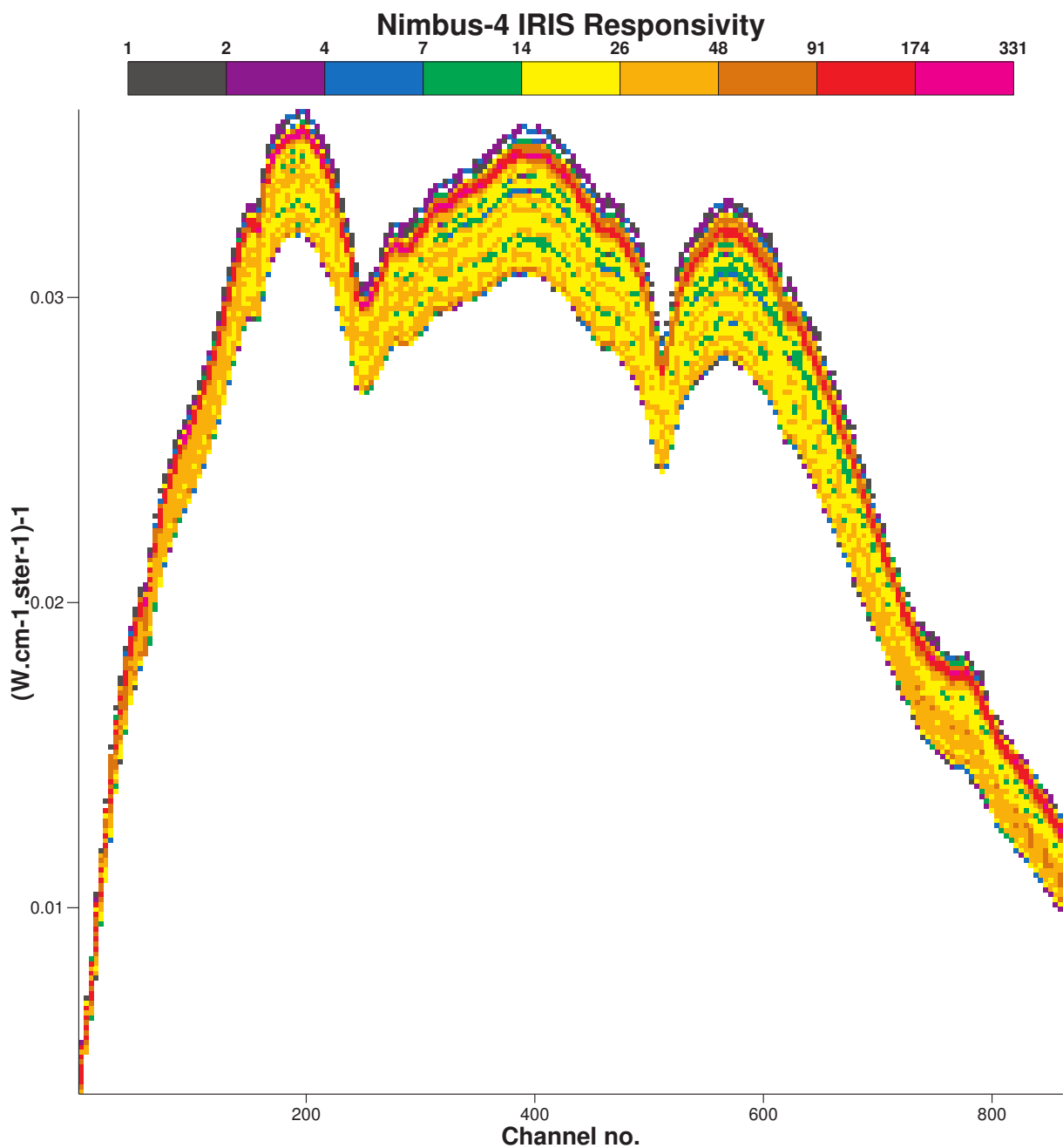
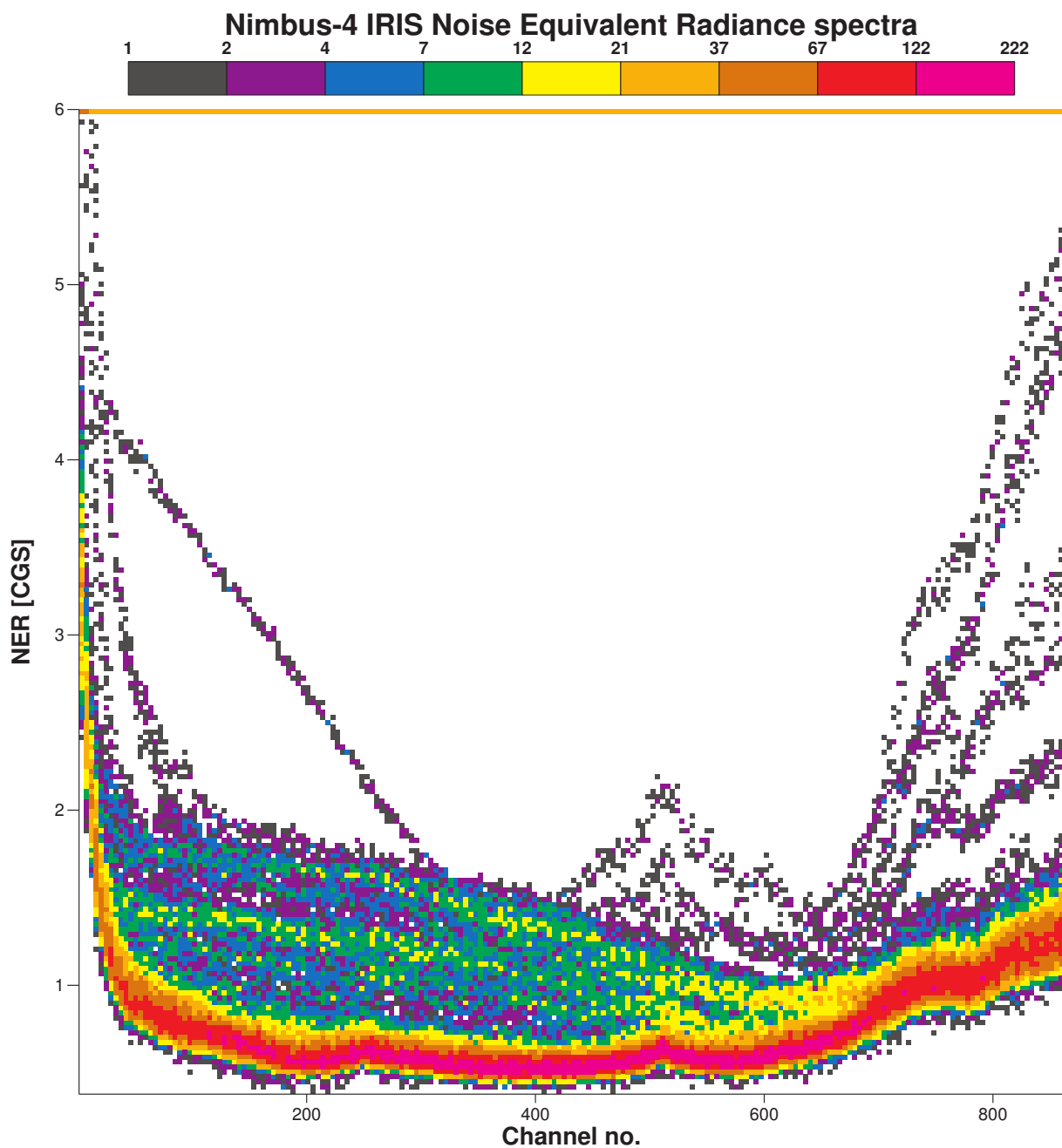*Figure 37: Average responsivity spectra (IRIS dataset record type 4)*

Figure 38: Instrument noise equivalent radiance spectra (IRIS dataset record type 5)

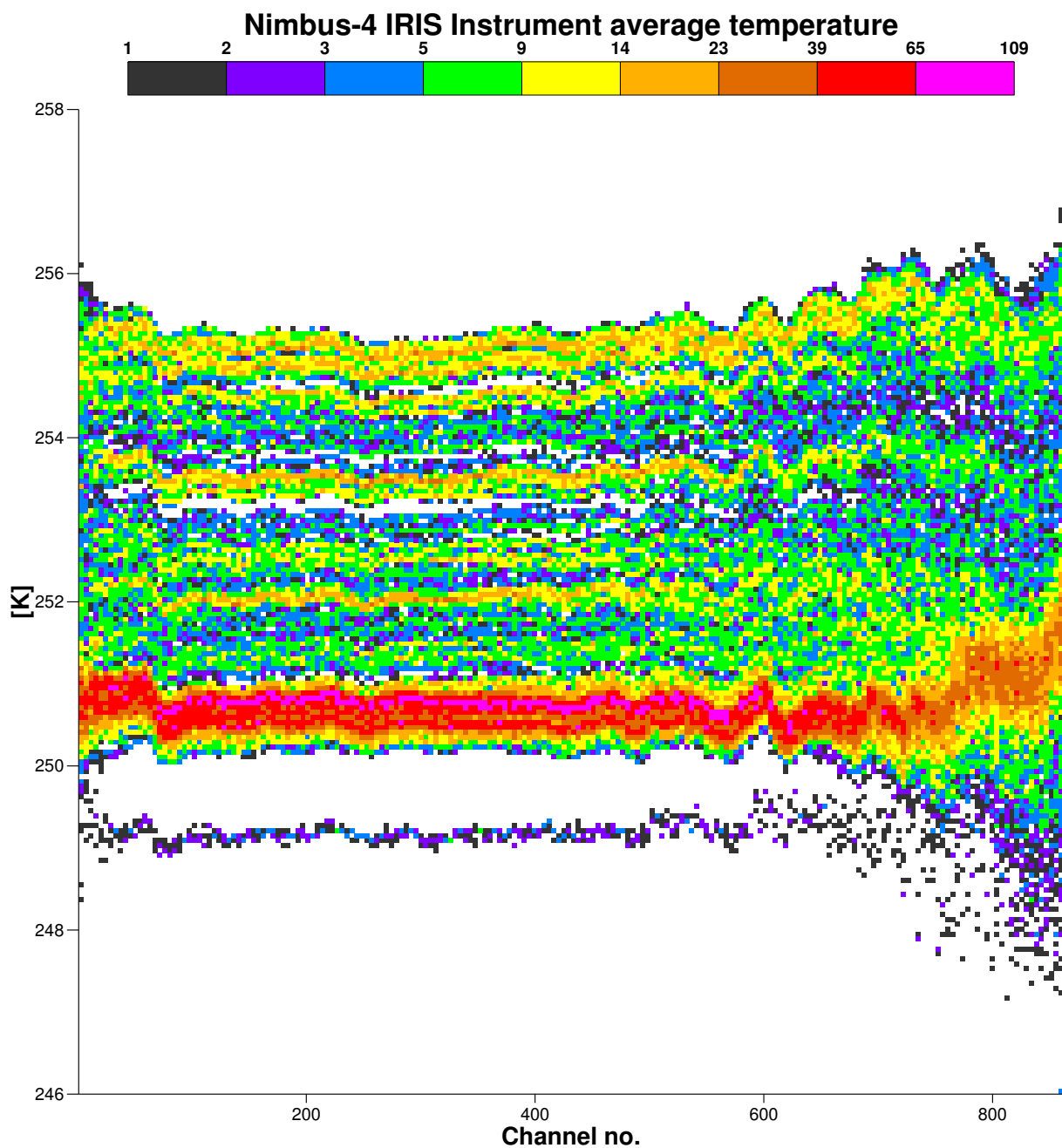## Nimbus-4 IRIS Instrument average temperature

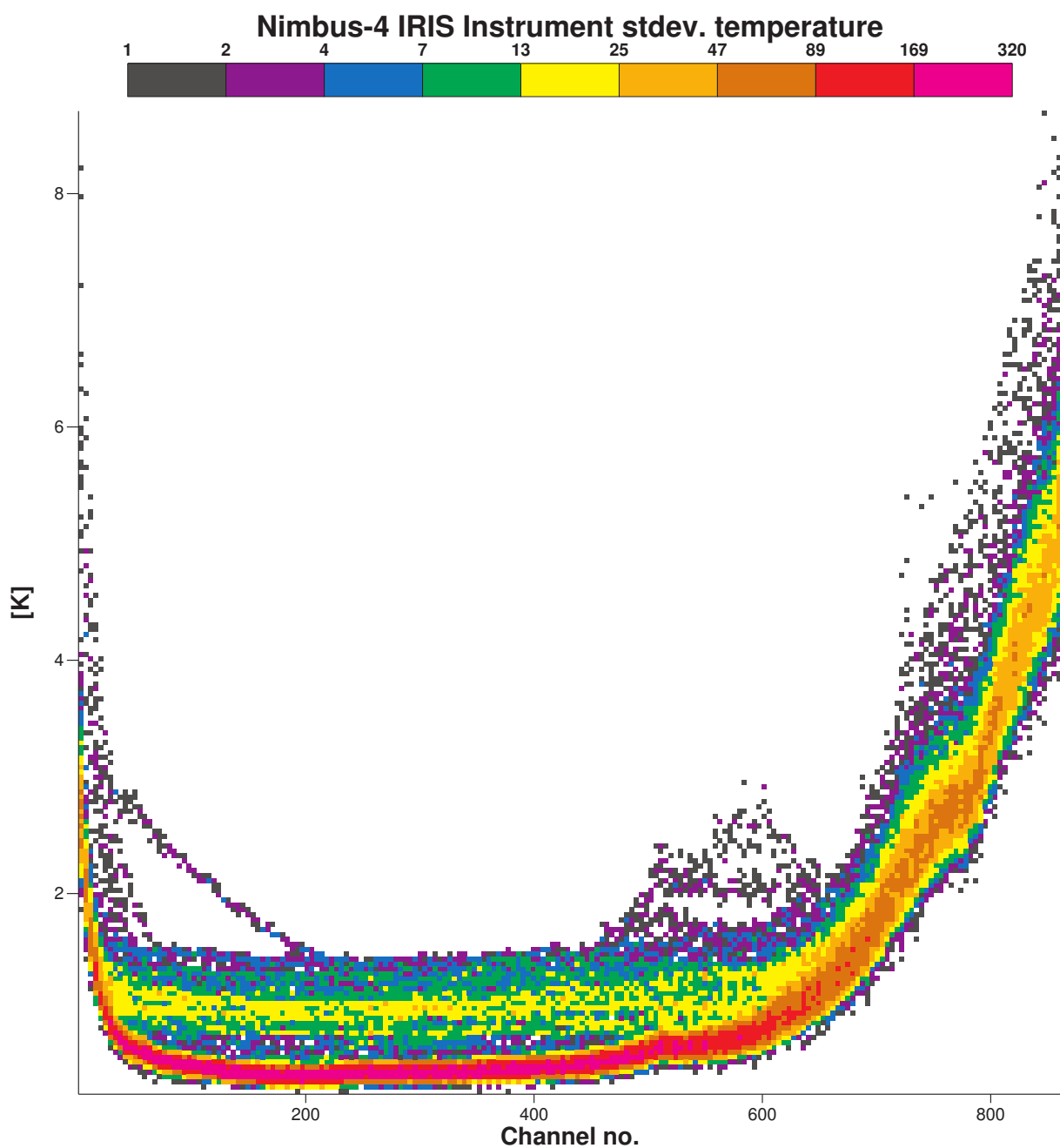*Figure 39: Instrument average temperature spectra (IRIS dataset record type 6)*

Figure 40: Instrument temperature standard deviation spectra (IRIS dataset record type 7)